

# Fibonacci Laws of Planetary Motion: From Solar System Architecture to Earth's Orbital Cycles

D. van Sonsbeek\*

*Independent Researcher, Den Dolder, The Netherlands*

May 20, 2026

## Abstract

Three major frameworks in planetary science — Kepler's orbital geometry, Milankovitch climate theory, and Laplace–Lagrange secular perturbation theory — describe planetary motion with high precision, yet no unifying principle connects precession timescales, orbital amplitudes, and the collective structure of the solar system. We present a geometric model in which two counter-rotating reference points, with periods in the Fibonacci ratio 13:3, generate a 335,317-year master cycle (the Earth Fundamental Cycle) from which Earth's major precession periods emerge as integer Fibonacci divisions. From this single timescale we identify 6 structural laws connecting the orbital inclinations and eccentricities of all eight planets through Fibonacci numbers: a Fibonacci cycle hierarchy for Earth's precession periods (Law 1), paired amplitude-constant and collective-balance laws on inclinations (Laws 2–3) and eccentricities (Laws 4–5), and a closed Saturn–Jupiter–Earth beat-frequency resonance (Law 6). All 6 laws require zero free parameters beyond the master cycle itself; two empirical constants ( $\psi$  for inclination amplitudes,  $K$  for eccentricity amplitudes) each derived from Earth predict all eight planets. Using J2000 orbital elements ( $a, m, i$  from JPL/DE440) and phase-derived base eccentricities (long-term oscillation midpoints), the inclination balance (Law 3) reaches 99.9975% and the eccentricity balance (Law 5) reaches 99.8632% — both from a single set of Fibonacci divisors with no forced constraints — and Law 5 predicts Saturn's eccentricity from the other seven planets to  $\sim 0.27\%$ . A joint permutation test over the 4 empirical laws yields  $p = 1.5 \times 10^{-4}$  (conservative) to  $p = 1.0 \times 10^{-6}$  (Monte Carlo), corresponding to  $3.62\text{--}4.75\sigma$ . A formation-epoch origin mechanism explains the observed precision, the five standard Milankovitch cycles emerge as  $H/n$  with Fibonacci-related indices, Saturn's observed ecliptic-retrograde perihelion precession receives a new explanation, and Earth is identified as the sole planet with prograde ICRF perihelion precession. A geocentric 3D simulation reproduces the positions of the Sun, Moon, and all eight planets — including Earth's own obliquity, eccentricity, and inclination — to  $< 0.09^\circ$  RMS against JPL Horizons ( $\sim 1800\text{--}2200$  AD). The framework produces testable consequences for Earth, including a unified obliquity formula, a reinterpretation of the 100,000-year glacial cycle as belonging to the inclination-side family of eigenmode beats — with empirical centroid at the Mercury–Mars  $s_1 - s_4$  nodal beat at 107.3 kyr (a planet-pair orbital-plane coupling, not an eccentricity beat) and the model's  $H/3$  inclination precession as one theoretical pathway within that family — supported by an explicit Orbital Forcing Formula (26 integer-divisor components fit on LR04,  $R^2 = 0.238$  — capturing the orbital-forcing component only, with the remaining  $\sim 76\%$  of LR04 variance arising from non-orbital climate-system response: ice-sheet hysteresis,  $\text{CO}_2$  and carbon-cycle feedbacks, internal variability), and a time-varying Mercury perihelion anomaly. The model generates 19 specific predictions; BepiColombo (science operations from 2027) and the Vera Rubin Observatory (LSST, 2025–2035) provide near-term discriminating tests. The model uses 6 adjustable parameters; all data, formulas, and a 3D simulation are publicly available.

**Keywords:** celestial mechanics, precession, obliquity, eccentricity, Milankovitch cycles, orbital dynamics, Fibonacci sequence, invariable plane, reference frame effects, BepiColombo, Mercury perihelion, angular momentum deficit, KAM theory

## 1. Introduction

### 1.1 The Missing Link

Modern astronomy describes planetary orbits with extraordinary precision, yet three major frameworks operate in isolation. Kepler's laws describe orbital geometry. Milankovitch theory describes Earth's climate cycles through eccentricity, obliquity, and precession. Laplace–Lagrange secular theory describes long-term orbital perturbations and angular momentum exchange. No framework connects the *timescales* of precession, the *amplitudes* of orbital inclinations and eccentricities, and the *collective structure* of the solar system within a single mathematical description.

This disconnection leaves fundamental questions unanswered. Why does Earth's obliquity oscillate at  $\sim 41k$  years? Why does eccentricity vary quasi-periodically? Why do

Fibonacci ratios appear in planetary period ratios (Pletser, 2019; Aschwanden, 2018)? Each question has partial answers within its own framework, but no unifying principle connects them.

### 1.2 Open Questions

Three long-standing problems motivate this work:

1. **The 100,000-year problem:** Geological records show a dominant  $\sim 100,000$ -year glacial cycle, but Milankovitch eccentricity provides only  $\sim 0.2\%$  insolation change — too weak without amplification mechanisms (Hays et al., 1976; Muller & MacDonald, 1997a). The theoretically dominant  $\sim 400,000$ -year eccentricity cycle is largely absent from climate records. This remains unsolved: Barker et al. (2025) continue to debate the distinct roles of precession, obliquity, and eccentricity, while the Mid-

Pleistocene Transition is described as “one of paleoclimatology’s great unsolved puzzles.”

2. **No unified precession framework:** Axial precession (luni-solar torque), apsidal precession (planetary perturbations), and obliquity variation (secular perturbations) share gravitational origins but are modeled independently (Capitaine et al., 2003; Laskar, 1993; Berger, 1988).
3. **No single-formula predictions:** Current models rely on polynomial fits to numerical integrations, valid over limited time ranges. Vondrák et al. (2011) extended IAU 2006 precession to  $\pm 200,000$  years — the state of the art. No closed-form solution exists for the gravitational  $n$ -body problem.

### 1.3 The Holistic Universe Model

The starting point is an empirical observation: two of Earth’s precession motions — axial and inclination — rotate in *opposite directions*, and their periods relate as a Fibonacci ratio (13:3). The same geometric construction — two reference points per planet — produces the analogous cycles for every planet. The Holistic Universe Model explores their collective structure within a geocentric 3D software simulation built from 6 adjustable parameters that reproduces all major solar system movements: invariable plane orientation, inclination and perihelion precession, eccentricity cycles, obliquity, and planetary orbits. All orbits use circular geometry with equation of center corrections and empirical parallax corrections fitted against JPL Horizons and historical transit/opposition reference data ( $\sim 1800$ – $2200$  AD), achieving RMS positional accuracy within  $0.09^\circ$  for all nine targets (Sun, Moon, and seven planets), with six under  $0.06^\circ$  (Sun, Moon, Venus, Jupiter, Uranus, Neptune).

The methodology is empirical-first: orbital parameters were measured from the simulation, exported to independent analysis tools, and only then were analytical formulas and structural laws identified from the numerical output. Two categories of results emerged. First, closed-form formulas for obliquity, eccentricity, precession rates, and day/year lengths at any epoch (the unified  $\sim 2,400$ -term predictive system, Section 12). Second, six Fibonacci Laws connecting all eight planets through Fibonacci numbers and a single timescale. The simulation serves as both discovery tool and independent test bed: established results such as the invariable plane orientation of Souami & Souchay (2012) can be verified within the same framework. The simulation is publicly available<sup>1</sup> and documented in full<sup>2</sup>.

The model does not claim to replace  $n$ -body gravitational theory. Rather, it proposes a geometric framework that captures regularities in the solar system’s dynamics not immediately visible in numerical integrations.

### 1.4 This Paper’s Contribution

We present 6 Fibonacci Laws of planetary motion derived from a geometric model of the solar system. The paper is organized in three parts:

- **Part I** (Sections 2–8): The Fibonacci structure — the model, the 6 laws, physical origin, statistical significance, and exoplanet evidence

- **Part II** (Sections 9–11): Consequences for Earth — observable Earth dynamics, the 100,000-year climate problem, and Mercury’s perihelion as a reference frame effect
- **Part III** (Sections 12–16): Predictions and validation — predictive formulas, calibration transparency, 19 testable predictions, and discussion

## Part I: The Fibonacci Structure

### 2. The Model: Two Counter-Rotating Reference Points

#### 2.1 Foundation

The model is built on two mathematical constructs — not physical objects, but reference points that parameterize known precession phenomena:

**EARTH-WOBBLE-CENTER:** A reference point near Earth, at a distance of 0.001356 AU. Earth traces its axial precession circle clockwise around this point (as seen from the north ecliptic pole). Period:  $\sim 25,794$  years. This represents the luni-solar precession.

**PERIHELION-OF-EARTH:** A reference point near the Sun, at a distance of 0.015386 AU. This point orbits counter-clockwise around the Sun, marking the direction of Earth’s closest approach. Period:  $\sim 111,772$  years. This represents the planetary precession.

The model recasts these as two counter-rotating circular motions within a single geometric framework (Fig. 1).

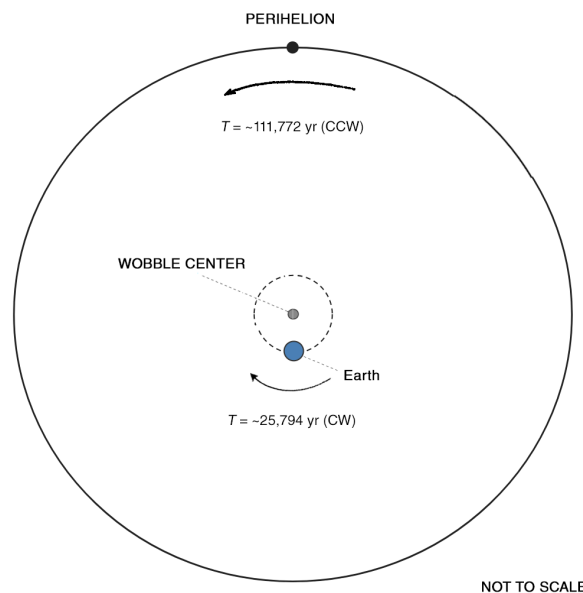


**Figure 1:** Schematic of the two counter-rotating reference points. Earth orbits the EARTH-WOBBLE-CENTER clockwise (CW) with period  $T \approx \sim 25,794$  years, while the PERIHELION-OF-EARTH orbits counter-clockwise (CCW) around the Sun with period  $T \approx \sim 111,772$  years. The 13:3 ratio produces the 335,317-year Earth Fundamental Cycle. Not to scale.

#### 2.2 The Fibonacci Ratio and KAM Theory

The ratio of the two fundamental periods is:

<sup>1</sup><https://3d.holisticuniverse.com>

<sup>2</sup><https://holisticuniverse.com>

$$\frac{T_{\text{incl}}}{T_{\text{axial}}} \approx \frac{\sim 111,772}{\sim 25,794} = 4.333 \dots = \frac{13}{3} \quad (1)$$

Both 3 and 13 are Fibonacci numbers ( $F_4$  and  $F_7$ ). This has theoretical grounding in the Kolmogorov–Arnold–Moser (KAM) theorem, which proves that orbital systems with “most irrational” frequency ratios are maximally stable against perturbation (Morbidelli & Giorgilli, 1995). The golden ratio  $\varphi \approx 1.618$ , to which successive Fibonacci ratios converge, is the most irrational number in a precise mathematical sense. Greene (1979) showed computationally that the golden-ratio torus is the last to break under perturbation. Pletser (2019) demonstrated that orbital period ratios preferentially cluster near Fibonacci fractions ( $\sim 60\%$  vs  $\sim 40\%$  for non-Fibonacci), and Aschwanden (2018) found Fibonacci fractions in 73% of 932 exoplanet pairs. The 13:3 ratio thus reflects a maximally stable configuration predicted by dynamical systems theory.

KAM theory explains why Fibonacci ratios are *preferred* — but not why they are realized so precisely. Across the 6 laws, Laws 1 and 6 are exact algebraic identities; using J2000 orbital elements ( $a$ ,  $m$ ,  $i$  from JPL/DE440) and phase-derived base eccentricities, Law 3 reaches 99.9975% inclination balance and Law 5 reaches 99.8632% eccentricity balance; Laws 2 and 4 predict all oscillation amplitudes from two empirical constants ( $\psi$  and  $K$ , both derived from Earth); and Law 5 predicts Saturn’s eccentricity from the other seven planets to  $\sim 0.27\%$ . The precision comes from the solar system’s formation epoch: dissipative forces in the protoplanetary disk drove orbits into the deepest Fibonacci stability wells, and disk dissipation froze the configuration in place. Section 7 presents the evidence for this formation-epoch mechanism.

### 2.3 The Earth Fundamental Cycle and Derived Cycles

The 13:3 ratio produces a master cycle, the Earth Fundamental Cycle:

$$H = 13 \times \sim 25,794 = 3 \times \sim 111,772 = 335,317 \text{ years} \quad (2)$$

All subsidiary cycles emerge as integer divisions of the Earth Fundamental Cycle (Table 1).

**Table 1:** Derived cycles from the Earth Fundamental Cycle (Law 1)

Cycle	Divisor	Duration (yr)	Fibonacci?
Earth Fundamental Cycle	1	335,317	$F_1 = 1$
Inclination Precession	3	$\sim 111,772$	$F_4 = 3$
Ecliptic Precession	5	$\sim 67,063$	$F_5 = 5$
Obliquity cycle	8	$\sim 41,915$	$F_6 = 8$
Axial precession	13	$\sim 25,794$	$F_7 = 13$
Perihelion precession	16	$\sim 20,957$	$13 + 3 = 16$

The perihelion precession period emerges from the meeting frequency of the two counter-rotating motions:

$$\begin{aligned} \frac{1}{T_{\text{perihelion}}} &= \frac{1}{T_{\text{axial}}} + \frac{1}{T_{\text{incl}}} \\ &= \frac{1}{\sim 25,794} + \frac{1}{\sim 111,772} = \frac{1}{\sim 20,957} \end{aligned} \quad (3)$$

The frequencies add (rather than subtract) because the motions are in opposite directions.

**Earth’s H/Fibonacci hierarchy is unique among the planets:** only Earth has all major precession periods at  $H$  divided by Fibonacci numbers (Law 1, Section 3). Jupiter’s perihelion ( $H/5$  ecliptic,  $H/8$  ICRF) and Saturn’s perihelion ( $H/8$  ecliptic,  $H/21$  ICRF) coincide with some of these Fibonacci values — but those specific coincidences are the subject of Law 6 (Section 6). The other planets’ precession periods divide the Solar System Resonance Cycle ( $8H$ , §2.5) by various integers, mostly non-Fibonacci.

### 2.4 The Balanced Year (Epoch Anchor)

The model uses a reference epoch called the Balanced Year, calculated from the last perihelion–solstice alignment:

$$T_{\text{balanced}} = 1246.03 \text{ AD} - 14.5 \times 20,957.31 = -302,635 \quad (4)$$

At this epoch (302,635 BC), the axial tilt and inclination tilt effects are in exact opposition, producing the Pythagorean mean obliquity of  $\sim 23.453^\circ$  (the geometric mean  $23.41354^\circ$  increased by perpendicular perihelion and ecliptic tilt components). The value is not arbitrary: within the 335,317-year cycle, the observed inclination trend (currently decreasing) and the observed obliquity trend (currently decreasing) must be simultaneously reproduced. Only a narrow range of phase offsets achieves this, and  $14.5 \times \sim 20,957$  emerged as the only configuration consistent with all observational constraints — the current rates of change, the J2000 values, and the known oscillation ranges. This serves as the phase-zero reference for all cycle calculations, analogous to how J2000 serves as the standard astronomical epoch.

### 2.5 The Solar System Resonance Cycle ( $8H$ )

The preceding subsections developed  $H$  as Earth’s master cycle. Each of the other seven planets has its own characteristic master period; all eight converge at a common super-period of eight Earth Fundamental Cycles — the Solar System Resonance Cycle:

$$8H = 2,682,536 \text{ years} \quad (5)$$

The same six kinds of cycles observed for Earth — axial precession, perihelion precession (ecliptic and ICRF), inclination oscillation, ascending-node regression, obliquity oscillation, and eccentricity oscillation — exist for every planet (visible in JPL ephemeris data and long-term integrations such as Laskar’s La2010 solution). What unifies them is that across all eight planets, every one of these cycles is an integer divisor of  $8H$ . After one Solar System Resonance Cycle ( $\sim 2.68$  million years), each planet returns to its starting configuration simultaneously across all six cycle types.

The Solar System Resonance Cycle plays three structural roles in the model:

- **Universal divisor:** Every planetary cycle period is expressible as  $8H/N$  for some integer  $N$ . For example, Earth’s axial precession ( $H/13$ ) is  $8H/104$ , its perihelion precession ( $H/16$ ) is  $8H/128$ , and its obliquity cycle ( $H/8$ ) is  $8H/64$ . This integer-divisor property holds for all eight planets and all six cycle types.

- **Ascending-node periods are integer divisors of  $8H$ :** each fitted planet's ascending-node regression period takes the form  $8H/N$  for an integer  $N$ , with Jupiter and Saturn locked to a shared  $N = 36$ . Across all 7 fitted planets, the  $8H/N$  integers reproduce JPL's J2000-fixed-frame ascending-node trends with a cumulative residual error of  $\sim 5.8''/\text{century}$  ( $\approx 0.8''/\text{century}$  per planet, Section 6.4).
- **Mean obliquity computation:** The analytical mean obliquity (Eq. 17) is defined as the time-average over  $8H$ , the period over which all cosine terms in the two-component obliquity formula return to their starting values.

### 3. Law 1: Fibonacci Cycle Hierarchy

Earth's major precession periods divide the Earth Fundamental Cycle  $H = 335,317$  by Fibonacci numbers —  $H/3$  (inclination),  $H/5$  (ecliptic),  $H/8$  (obliquity),  $H/13$  (axial). The Fibonacci addition rule connects them:  $3 + 5 = 8$ ,  $5 + 8 = 13$ .

The resulting periods (Table 1) obey a beat-frequency rule inherited from the Fibonacci recurrence  $F_n + F_{n+1} = F_{n+2}$ :

$$\frac{1}{H/F_n} + \frac{1}{H/F_{n+1}} = \frac{1}{H/F_{n+2}} \quad (6)$$

Any two consecutive Fibonacci periods combine to produce the next. The entire hierarchy is generated by the interaction of just two physical periods — the axial precession ( $H/13$ ) and the inclination precession ( $H/3$ ) — through successive beat frequencies. Law 6 (Section 6) reveals the physical mechanism behind this hierarchy.

### 4. Laws 2–3: Inclination Structure

#### 4.1 Mass-Weighted Variables and AMD

The planetary data reveals deeper structure when expressed in mass-weighted variables:

- Mass-weighted eccentricity:  $\xi = e \times \sqrt{m}$
- Mass-weighted inclination amplitude:  $\eta = \text{amplitude} \times \sqrt{m}$

The square root of mass is not arbitrary — it is the unique exponent arising from the Angular Momentum Deficit (AMD) decomposition, the key conserved quantity governing long-term orbital stability (Laskar, 1997). A numerical scan over all mass exponents from 0 to 1 supports this: the products  $d \times \eta$  across all eight planets converge to a single value only at exponent 0.50, with a relative spread of 0.11%. No other exponent achieves a spread below 28%.

#### 4.2 The Invariable Plane

The invariable plane — perpendicular to the solar system's total angular momentum vector, dominated by Jupiter ( $\sim 60\%$ ) and Saturn ( $\sim 25\%$ ) — serves as the model's spatial reference. Unlike the ecliptic, which itself precesses, the invariable plane is fixed in inertial space. When measured against it, all planetary inclinations show smooth, predictable oscillations (Table 2).

Determining which  $d$ -value belongs to each planet requires an exhaustive search over 7,558,272 assignments, narrowed by five physical filters to 42 viable candidates — of which only one is mirror-symmetric (Section 4.5). That solution predicts that Jupiter's period equals the ecliptic precession

**Table 2:** Planetary inclination oscillations relative to the invariable plane

Planet	$d$	J2000 (°)	Mean (°)	Ampl. (°)	Ecliptic period (yr)	ICRF period (yr)
Mercury	21	6.347	6.703206	$\pm 0.386477$	243,867	-28,844
Venus	34	2.155	2.151359	$\pm 0.062165$	-447,089	-24,387
Earth	3	1.579	1.48113	$\pm 0.63603$	$\sim 20,957$	+11,772
Mars	5	1.631	1.915103	$\pm 1.164214$	76,644	-38,877
Jupiter	5	0.322	0.319552	$\pm 0.021404$	67,063	-41,915
Saturn	3	0.925	0.982896	$\pm 0.065192$	$\sim 41,915$	-15,967
Uranus	21	0.995	1.015182	$\pm 0.023831$	$\sim 111,772$	-33,532
Neptune	34	0.735	0.743803	$\pm 0.013551$	670,634	-26,825

$d$  is the planet's Fibonacci divisor in the inclination constant (Law 2):  $d \times \text{amp} \times \sqrt{m} = \psi$ . Earth and Saturn share  $d = 3$  (mirror pair); Mars and Jupiter share  $d = 5$ ; Mercury and Uranus share  $d = 21$ ; Venus and Neptune share  $d = 34$ .

and Saturn's equals the obliquity cycle — suggesting these planets drive the corresponding Earth cycles.

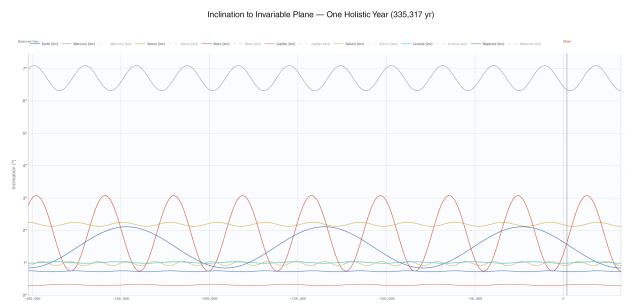


**Figure 2:** Inclination oscillations of all eight planets relative to the invariable plane over one Earth Fundamental Cycle ( $H = 335,317$  yr), shown at their ICRF perihelion periods. Mars has the largest amplitude and completes  $\sim 8.6$  cycles; Earth completes 3 cycles ( $H/3$ ); Saturn completes 21 cycles ( $H/21$  in ICRF), the highest of any planet; Jupiter completes exactly 8 cycles ( $H/8$ ).

#### 4.3 Law 2: The Inclination Constant

Each planet's mass-weighted inclination amplitude, multiplied by a Fibonacci quantum number, equals the same universal constant.

Defining  $\eta = \text{amplitude} \times \sqrt{m}$ , every planet satisfies:

$$d \times \eta = \psi \quad (7)$$

where  $d$  is a Fibonacci integer specific to each planet. The constant  $\psi$  is empirical, derived from Earth's fitted inclination amplitude:

$$\psi = d_E \times \text{amp}_E \times \sqrt{m_E} = 3.3068 \times 10^{-3} \quad (8)$$

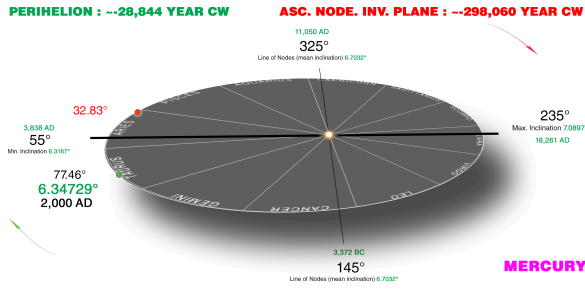
With zero free parameters, the model predicts inclination amplitudes for all eight planets (Table 3).

All eight predicted ranges fall within the bounds of Laplace–Lagrange secular theory, verified for all 42 surviving configurations in the selection pipeline (Section 4.5). The divisors (3, 5, 21, 34) are all Fibonacci numbers.

#### 4.4 Mirror Symmetry

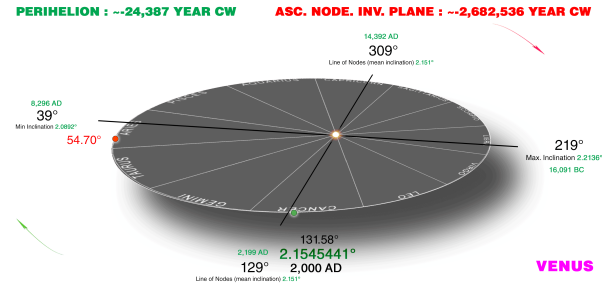
Each inner planet shares its quantum number  $d$  with its outer counterpart across the asteroid belt: Mercury–Uranus ( $d =$

### THE INVARIABLE PLANE



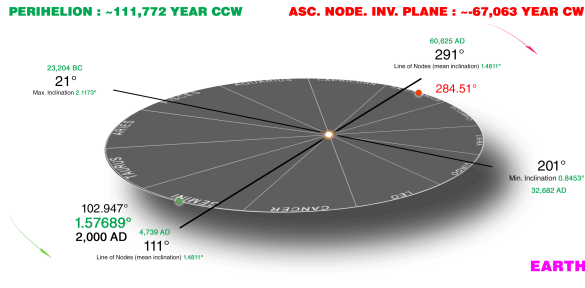
(a) Mercury (ecl: 243, 867 yr; ICRF: -28, 844 yr)

### THE INVARIABLE PLANE



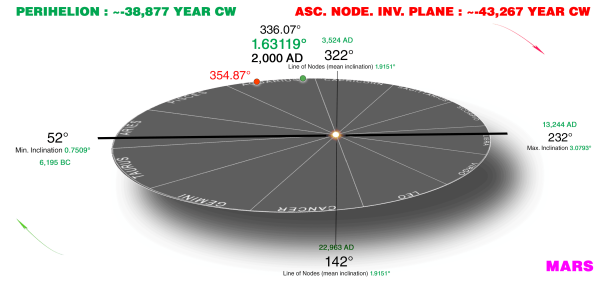
(b) Venus (ecl: -447, 089 yr; ICRF: -24, 387 yr)

### THE INVARIABLE PLANE



(c) Earth (ecl: ~20, 957 yr; ICRF: +111, 772 yr)

### THE INVARIABLE PLANE



(d) Mars (ecl: 76, 644 yr; ICRF: -38, 877 yr)

**Figure 3:** Perihelion and ascending node precession relative to the invariable plane — inner planets. Each panel shows one complete inclination oscillation cycle. The inclination oscillation is driven by the **ICRF perihelion longitude** (green dot), with per-planet inclination cycle anchors. The ascending node precesses on the invariable plane at a different rate; its role is to set the direction of the angular momentum perturbation vector that determines the vector balance. **Earth (panel c) is the only planet whose ICRF perihelion rate is prograde**, because Earth’s ecliptic apsidal rate ( $H/16$ ) exceeds the general precession ( $H/13$ ).

**Table 3:** Law 2: Inclination constant predictions

Planet	$d$	Fibonacci	Predicted amp	Mirror pair
Mercury	21	$F_8$	$0.386477^\circ$	$\leftrightarrow$ Uranus
Venus	34	$F_9$	$0.062165^\circ$	$\leftrightarrow$ Neptune
Earth	3	$F_4$	$0.63603^\circ$	$\leftrightarrow$ Saturn
Mars	5	$F_5$	$1.164214^\circ$	$\leftrightarrow$ Jupiter
Jupiter	5	$F_5$	$0.021404^\circ$	$\leftrightarrow$ Mars
Saturn	3	$F_4$	$0.065192^\circ$	$\leftrightarrow$ Earth
Uranus	21	$F_8$	$0.023831^\circ$	$\leftrightarrow$ Mercury
Neptune	34	$F_9$	$0.013551^\circ$	$\leftrightarrow$ Venus

**Table 4:** Selection pipeline

Filter	Surviving
Total search space	7,558,272
Inclination balance $\geq 99.994\%$	766
+ Eccentricity balance $\geq 99\%$	96
+ Optimised anchor gives LL bounds 8/8	51
+ Direction match, rate error $\leq 6''$	42
+ Mirror symmetry	<b>1</b>

21), Venus–Neptune ( $d = 34$ ), Earth–Saturn ( $d = 3$ ), Mars–Jupiter ( $d = 5$ ). This mirror symmetry reflects the block-diagonal structure of the secular coupling matrix, with the asteroid belt acting as a dynamical barrier.

#### 4.5 Configuration Selection

Each planet needs a Fibonacci divisor  $d$  and a balance group (in-phase or anti-phase). Earth is locked at  $d = 3$ ; Jupiter and Saturn are constrained by Law 6. The remaining five planets each have  $9 \times 2 = 18$  options, giving 7,558,272 candidates across four Jupiter–Saturn scenarios. Five successive physical filters narrow these to a single mirror-symmetric solution:

**Methodology.** The first two filters depend only on  $d$ -values. The LL-bounds and direction checks depend on two additional parameters: the **anchor position**  $n \in \{0, \dots, 7\}$

(which of eight equally-spaced points in  $8H$  defines the balanced year, setting all inclination cycle anchors) and the **ascending node integer**  $N$  per planet ( $\Omega$  regression period =  $-8H/N$ ). Each candidate is evaluated at its own optimal  $(n, N)$ . Jupiter and Saturn share the same  $N$  to preserve lock-step regression.

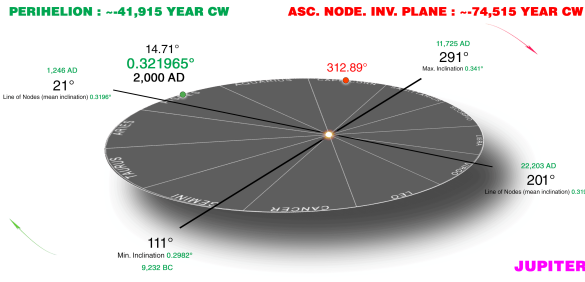
**Result.** Of 42 survivors, **only one is mirror-symmetric**: Me=21, Ve=34, Ma=5, Ju=5, Sa=3, Ur=21, Ne=34 (Config #11, ranked #11 of 42 by eccentricity balance at 99.8632%). Its anchor is  $n = 7$  with Jupiter–Saturn  $N = 36$ .

#### 4.6 Physical Meaning of $\psi$ : Mass-Independent Energy Partition

Substituting Law 2 (amp =  $\psi/(d\sqrt{m})$ ) into the standard AMD gives each planet’s inclination oscillation AMD:

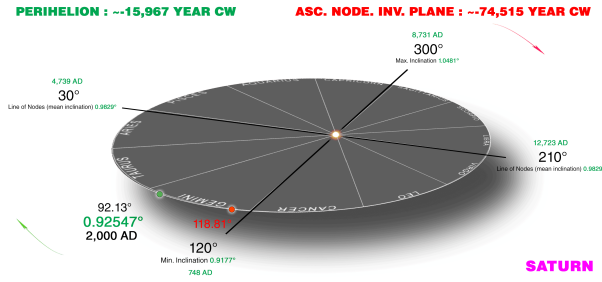
$$AMD_{incl} = \frac{m\sqrt{a}}{2} \left( \frac{\psi}{d\sqrt{m}} \right)^2 = \frac{\sqrt{a}\psi^2}{2d^2} \quad (9)$$

### THE INVARIABLE PLANE



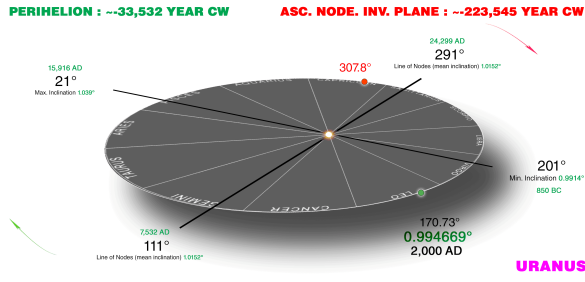
(a) Jupiter (ecl: 67, 063 yr; ICRF: -41, 915 yr)

### THE INVARIABLE PLANE



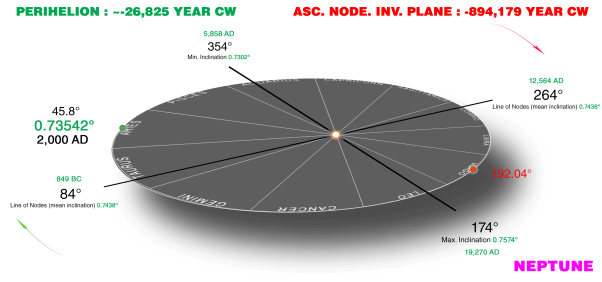
(b) Saturn (ecl: -41, 915 yr; ICRF: -15, 967 yr)

### THE INVARIABLE PLANE



(c) Uranus (ecl: ~111, 772 yr; ICRF: -33, 532 yr)

### THE INVARIABLE PLANE



(d) Neptune (ecl: 670, 634 yr; ICRF: -26, 825 yr)

**Figure 4:** Perihelion and ascending node precession relative to the invariable plane — outer planets. Saturn (panel b) precesses clockwise (CW) in the ecliptic frame, caused by Jupiter’s gravitational pull from inside its orbit. Saturn is **anti-phase**: its cosine sign is flipped relative to all other planets — making it the sole counterweight in the inclination balance (Law 3).

Mass cancels exactly. Law 2 appears to depend on mass — heavier planets tilt less — but this apparent mass dependence is precisely what removes mass from the energy budget:  $\sqrt{m}$  is the unique exponent that makes this cancellation work. Each planet’s inclination oscillation energy depends only on its orbital distance ( $\sqrt{a}$ ) and Fibonacci quantum number ( $d$ ), not on how massive the planet is.

**Table 5:** Inclination oscillation energy shares ( $\propto \sqrt{a}/d^2$ )

Planet	$d$	$\sqrt{a}/d^2$	Share
Mercury	21	0.0014	0.2%
Venus	34	0.0007	0.1%
<b>Earth</b>	<b>3</b>	<b>0.1111</b>	<b>18.2%</b>
Mars	5	0.0494	8.1%
Jupiter	5	0.0912	14.9%
<b>Saturn</b>	<b>3</b>	<b>0.3430</b>	<b>56.1%</b>
Uranus	21	0.0099	1.6%
Neptune	34	0.0047	0.8%

The divisor  $d$  acts as an energy quantum number (Table 5): higher  $d$  means less oscillation energy, scaling as  $1/d^2$ . Saturn dominates (56%) not because of mass (Jupiter is 3× heavier) but because  $d = 3$  combined with a large orbit maximises  $\sqrt{a}/d^2$ . Earth carries more oscillation energy than Jupiter (18% vs 15%) despite being ~1000× lighter. The Earth–Saturn pair ( $d = 3$ ) carries 74% of the eight-planet total; the E–J–S resonance triad (Law 6) carries 89%. (Shares are relative to the eight major planets, which carry 99.994% of the system’s orbital angular momentum; TNOs contribute the re-

mainder (Li et al., 2019).)

The same structural properties that make Saturn the dominant energy carrier —  $d = 3$  and a large orbit — also make it the sole counterweight in the inclination balance (Law 3, §4). In this mass-independent partition Saturn carries 56%; in the mass-dependent balance of Law 3, Saturn carries exactly 50% (by definition it equals the other seven combined). The gap is absorbed by mass: Jupiter is 3.3× heavier than Saturn, boosting Jupiter’s balance weight relative to its energy share and redistributing the load from 56/44 to an exact 50/50 split.

Summing over all planets yields a budget equation that determines  $\psi$ ’s magnitude:

$$\psi^2 = \frac{2 \times \text{AMD}_{\text{incl}}^{\text{total}}}{\sum_j \sqrt{a_j} / d_j^2} \tag{10}$$

This fixes  $\psi$  from two formation-epoch quantities: the total inclination oscillation energy and the geometric sum  $\sum \sqrt{a}/d^2$  set by Fibonacci structure and Kepler spacing. An identical mass cancellation holds for eccentricity via Law 4:  $\text{AMD}_{\text{ecc}} = \sqrt{a} \xi^2/2$ , where  $\xi = e \sqrt{m}$ .

#### 4.7 The Inclination Oscillation Mechanism

Each planet’s inclination to the invariable plane oscillates with the ICRF perihelion longitude:

$$i(t) = \bar{i} + A \cos(\omega_{\text{ICRF}}(t) - \varphi) \tag{11}$$

where  $\omega_{\text{ICRF}}(t)$  is the ICRF perihelion longitude (ecliptic

rate minus general precession  $H/13$ ) and  $\varphi$  is a per-planet **in-clination cycle anchor** — the ICRF perihelion longitude at which the planet reaches its inclination extremum (maximum for in-phase planets, minimum for Saturn). Each anchor is set by the System Reset epoch ( $\sim 2,649,854$  BC,  $n = 7$ ). Saturn is anti-phase: its cosine sign is flipped relative to the other seven planets. Earth is the sole planet with prograde ICRF perihelion motion ( $+H/3$ ); all others are retrograde. All ICRF periods divide  $8H = 2,682,536$  years (the Solar System Resonance Cycle), meaning the full anti-phase alignment — Saturn at maximum while all others at minimum — occurs once per  $8H$ .

**The role of the ascending node.** The ascending node  $\Omega_{inv}$  also precesses on the invariable plane, but at a different rate than the ICRF perihelion. The two play complementary roles: the **ICRF perihelion longitude drives the magnitude** of each planet’s inclination oscillation (it appears inside the cosine in Eq. (11) above), while the **ascending node sets the direction** of the angular momentum perturbation vector  $\vec{P}_j = L_j \sin(i_j)(\sin \Omega_j, \cos \Omega_j)$  that determines the vector balance of the invariable plane. Both quantities are needed: the inclination phase is what oscillates over time, and the ascending node direction is what makes the vectors cancel as 2D quantities.

**4.8 Law 3: The Inclination Balance**

*The angular-momentum-weighted inclination oscillations of seven planets balance against Saturn’s alone, conserving the orientation of the invariable plane.*

Each planet’s orbital tilt oscillates with a per-planet inclination cycle anchor (ICRF perihelion longitude at the System Reset, where the planet reaches its inclination extremum). The balance requires two groups:

- **In-phase group:** Mercury, Venus, Earth, Mars, Jupiter, Uranus, Neptune — cosine sign positive
- **Anti-phase group:** Saturn (alone) — cosine sign flipped

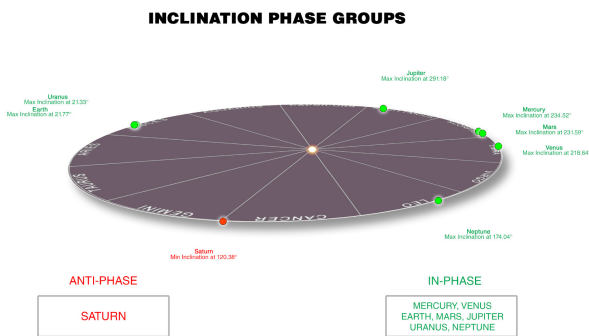


**Figure 5:** Inclination balance groups on the invariable plane. Seven in-phase planets (green) have positive cosine sign; Saturn alone (red, anti-phase) has flipped sign. The angular-momentum-weighted oscillations of the two groups cancel exactly.

Saturn’s orbital angular momentum — amplified by its large distance from the Sun — single-handedly balances the other seven planets combined. Using the structural weight

$w_j = \sqrt{m_j \cdot a_j(1 - e_j^2)}/d_j$  with phase-derived base eccentricities, the inclination balance is 99.9975%. The same Fibonacci divisors and phase assignments simultaneously produce an independent eccentricity balance of 99.8632% (Law 5).

**Scalar vs vector balance.** Law 3 is a *scalar* balance condition: it requires that the structural weights  $w_j$  of the in-phase and anti-phase groups cancel exactly. This is the genuine physical constraint that selects the unique Fibonacci  $d$ -value configuration. A separate question is whether the angular momentum perturbation *vectors* (each planet’s  $L \times \sin i$  acting along its ascending node direction) cancel as 2D vectors at all times — not just on average. The vector cancellation is guaranteed by the eigenmode structure of secular perturbation theory: the invariable plane is by definition the plane where these vectors sum to zero, and any decomposition of the planetary orbits into eigenmodes (e.g., the seven Laplace–Lagrange secular modes  $s_1$ – $s_8$  with  $s_5 = 0$ ) automatically preserves this cancellation. The  $d$ -value selection (Law 3 + Law 5, scalar) and the vector cancellation (eigenmode structure) operate independently and address different aspects of the same physics.

**5. Laws 4–5: Eccentricity Structure**

**5.1 Law 4: The Eccentricity Amplitude Constant**

*A single constant  $K$  predicts all eight eccentricity oscillation amplitudes from Fibonacci divisors, mass, distance, and axial tilt.*

Each planet’s eccentricity oscillates around a base value over its eccentricity cycle. The oscillation amplitude follows a universal formula:

$$e_{amp} = K \times \frac{\sin(\text{tilt}) \times \sqrt{d}}{\sqrt{m} \times a^{3/2}} \tag{12}$$

$K = 3.4149 \times 10^{-6}$ , derived from Earth’s eccentricity amplitude and axial tilt. This is the eccentricity analog of  $\psi$  (Law 2) — a single constant, zero free parameters, all eight planets predicted. Both  $\psi$  and  $K$  are empirical constants derived from Earth.  $K$  additionally uses semi-major axis and axial tilt, coupling the spin and orbital domains.

**Note on base eccentricities.** Laws 2 and 4 predict oscillation *amplitudes*. The base (mean) eccentricities are partially constrained by Law 5, which predicts Saturn’s from the other seven. The remaining seven base eccentricities are structural values set at formation.

**5.2 Law 5: The Eccentricity Balance**

*An independent balance condition on eccentricities holds using the same Fibonacci divisors and phase groups, with Saturn alone balancing the other seven planets.*

Each planet receives an eccentricity weight  $v_j = \sqrt{m_j} \times a_j^{3/2} \times e_j / \sqrt{d_j}$ . The weights for the seven in-phase planets sum to match Saturn’s weight alone:

**Balance:** 99.8632% (base eccentricities); 99.8753% (J2000 eccentricities)

With base eccentricities derived from the **System Reset phase** ( $n=7$ , with balance-group offsets:  $90^\circ$  for in-phase

planets, 270° for Saturn) (Table 6), the eccentricity balance reaches 99.8632% — naturally, with no forced constraints. This is genuinely independent of Law 3: eccentricity weights differ from inclination weights by over 100-fold for some planets, yet both conditions are simultaneously satisfied by the same Fibonacci divisors. Three tests confirm it depends on the actual eccentricity values: without eccentricities the balance drops to 74%; random eccentricities give only 50–85%; and the balance peaks at linear eccentricity, dropping for other powers.

Base eccentricities for the seven non-Earth planets are derived from the System Reset phase anchor (n=7) with balance-group phase offsets: in-phase planets at phase 90° (mean, rising), Saturn at phase 270° (mean, falling) at the anchor. Earth’s base is independently determined by the Sun optimizer from its two-vector scene-graph geometry. The eccentricity oscillation phase at J2000 determines each planet’s base from its observed J2000 eccentricity. Venus shows the largest base-to-J2000 offset (+13.7%), indicating it is well away from its oscillation midpoint at the current epoch. Mars’s base is –2.1% relative to its J2000 value. The outer planets are essentially at their midpoints (< 0.1%) because their *K*-derived amplitudes are negligible relative to their base eccentricities (Table 6).

**Table 6:** Phase-derived base eccentricities

Planet	Base <i>e</i>	vs. J2000
Mercury	0.20563	< 0.01%
Venus	0.00771	+13.7%
Earth	0.01539	–7.9%
Mars	0.09146	–2.1%
Jupiter	0.04839	< 0.01%
Saturn	0.05387	< 0.01%
Uranus	0.04724	–0.03%
Neptune	0.00860	+0.07%

**The ~0.14% residual.** The eccentricity balance reaches 99.8632% but not exactly 100%. The residual may reflect contributions from minor bodies (dwarf planets, asteroids) not included in the 8-planet framework, or measurement uncertainties in planetary masses — particularly Uranus and Neptune, whose masses are known only from Voyager 2 fly-bys (relative uncertainties ~0.02–0.08%). A future Uranus or Neptune orbiter mission providing more precise mass measurements should improve the balance — this is a testable prediction.

**Saturn from Law 5 alone.** Law 5 derives Saturn’s eccentricity from the global balance equation involving all eight planets simultaneously:  $e_{\text{Saturn}} = 0.053719$  (predicted from the other seven planets; –0.27% from the model midpoint of 0.053866). Saturn’s eccentricity oscillates secularly between ~0.01 and ~0.09 — a factor-of-9 dynamic range — and is the only planetary eccentricity currently derivable from the model. The Fibonacci divisors were originally chosen to match precession periods (Law 1) and inclination balance (Law 3); the Saturn eccentricity prediction was never optimized for. Predicting the remaining seven *base* eccentricities (Law 4, Section 5.1, currently covers oscillation amplitudes only) is open work for a future extension.

### 5.3 Eccentricity Amplitude Constant *K*

While no universal constant exists for base eccentricities, the eccentricity *amplitude* follows a universal formula:

$$e_{\text{amp}} = K \times \frac{\sin(\text{mean obliquity}) \times \sqrt{d}}{\sqrt{m} \times a^{3/2}} \quad (13)$$

where  $K = 3.4149 \times 10^{-6}$ , derived from Earth’s mean obliquity (23.41354°) and eccentricity amplitude (0.001356). Each planet uses its own model mean obliquity (the time-averaged axial tilt, not the J2000 instantaneous value). This is the eccentricity analog of  $\psi$ : where  $\psi$  determines each planet’s inclination amplitude, *K* determines each planet’s eccentricity amplitude. Both are empirical constants derived from Earth, and both predict all 8 planets with zero free parameters. *K* additionally uses semi-major axis and axial tilt, coupling the spin and orbital domains. This coupling is bidirectional: a planet’s mean obliquity determines its eccentricity amplitude, and its eccentricity amplitude reveals its obliquity. Together,  $\psi$  and *K* link all three oscillation parameters — inclination amplitude, eccentricity amplitude, and axial tilt — through just two constants. Together with the base eccentricities from Laws 4–5, the full eccentricity at any time is:

$$e(t) = \sqrt{e_{\text{base}}^2 + e_{\text{amp}}^2} + (-e_{\text{amp}} - h_1 \cos \theta) \cos \theta \quad (14)$$

where  $\theta = 360^\circ \times (t - t_0)/T_{\text{cycle}}$  and  $h_1 = \sqrt{e_{\text{base}}^2 + e_{\text{amp}}^2} - e_{\text{base}}$ .

**Tilt prediction.** Inverting the formula — using JPL J2000 eccentricities to predict obliquities — provides an independent cross-check for all planets.

**Balance preservation.** The Law 5 eccentricity weight change from oscillation simplifies to  $\delta v = K \times \sin(\text{tilt})$  — mass and distance cancel completely. This ensures the eccentricity balance is preserved at every epoch, not just at the formation snapshot.

## 6. Law 6: Saturn-Jupiter-Earth Resonance

*Earth’s H/8 obliquity cycle equals both Jupiter’s ICRF perihelion period and Saturn’s ecliptic perihelion period — a triple identity at H/8 by which the gas giants gravitationally drive Earth’s spin-axis dynamics. Jupiter and Saturn maintain this configuration through their well-known mutual resonance lock.*

Saturn’s **anti-phase** role (its cosine sign flipped relative to the other seven planets) makes it the natural pivot for both balance laws (Laws 3 and 5). Three beat-frequency relationships form a closed triangle:

**Table 7:** Law 6: Saturn-Jupiter-Earth beat-frequency resonance

Beat relationship	Fibonacci	Physical meaning
$\frac{1}{H/3} + \frac{1}{H/5} = \frac{1}{H/8}$	3 + 5 = 8	Earth incl. + Jupiter → obliquity (Saturn)
$\frac{1}{H/8} - \frac{1}{H/5} = \frac{1}{H/3}$	8 – 5 = 3	Saturn – Jupiter → Earth inclination
$\frac{1}{H/8} - \frac{1}{H/3} = \frac{1}{H/5}$	8 – 3 = 5	Saturn – Earth → Jupiter

All three rows are cyclic permutations of a single Fibonacci identity: 3 + 5 = 8. Each planet’s period equals the

beat frequency of the other two — Saturn ( $H/8$ ) is the sum of Earth and Jupiter, Jupiter ( $H/5$ ) is Saturn minus Earth, and Earth ( $H/3$ ) is Saturn minus Jupiter. This also links to Law 1’s higher-level identity  $5 + 8 = 13$ : combining Jupiter ( $H/5$ ) and Saturn ( $H/8$ ) produces Earth’s axial precession ( $H/13$ ), extending the triangle into the full cycle hierarchy.

### 6.1 Saturn’s Ecliptic-Retrograde Perihelion Precession

JPL’s WebGeoCalc tool — which computes geometric quantities directly from the SPICE ephemeris kernels — shows that Saturn’s longitude of perihelion ( $\varpi = \Omega + \omega$ ) is **decreasing** over the period 1900–2000 AD at approximately  $-3,400''/\text{cy}$ . The ascending node regresses faster than the argument of perihelion advances, producing a net retrograde motion. The JPL Keplerian elements table (Standish & Williams, 1992) confirms  $d\varpi/dt = -0.419^\circ/\text{cy}$  in the 1800–2050 fit — the only gas giant with a negative rate.

**The standard explanation: the Great Inequality.** Standard celestial mechanics attributes this to a transient phase of the Great Inequality — the  $\sim 900$ -year oscillation from the near-5:2 mean-motion resonance of Jupiter and Saturn. The history: Kepler first noticed positional discrepancies ( $\sim 1625$ ); Halley quantified the drift ( $\sim 1695$ ); Euler and Lagrange failed to explain it (1748, 1766); Laplace solved it in 1784–1786, showing it was periodic, not secular (Wilson, 1985). Under this theory, the long-term secular rate is prograde at  $\sim +19.5''/\text{yr}$ , dominated by  $g_6 = 28.245''/\text{yr}$ , and the current retrograde motion is a temporary oscillation.

**Why the standard explanation is incomplete.** (1) No complete 900-year cycle of Saturn’s *perihelion* precession has ever been observed; the Great Inequality was derived from mean longitude, not  $\varpi$ . (2) The observed rate ( $\sim -3,400''/\text{cy}$ ) differs from the predicted secular rate ( $+1,950''/\text{cy}$ ) by  $\sim 5,350''/\text{cy}$  with opposite sign. (3) Iorio (2009) showed that no standard physics — not planetary perturbations, solar oblateness, asteroid belt mass, trans-Neptunian objects, general relativity, or modified gravity — can explain even a tiny retrograde residual detected in EPM2008 ( $-6 \pm 2 \text{ mas}/\text{cy}$ ).

**The model’s explanation.** Saturn’s perihelion precesses ecliptic-retrograde *permanently* with period  $H/8 = \sim 41,915$  years. The heliocentric rate is  $360^\circ/\sim 41,915 \approx -3,092''/\text{cy}$ ; adding the missing advance of perihelion ( $\sim -280''/\text{cy}$ ) gives a geocentric rate of  $\sim -3,372''/\text{cy}$ , matching the observed  $\sim -3,400''/\text{cy}$ . This ecliptic-retrograde motion is what makes Saturn the unique pivot: it enables both the 7-vs-1 balance (Laws 3 and 5) and the closed beat-frequency triangle ( $3+5 = 8$ ).

**Table 8:** Saturn’s perihelion: two competing theories

Aspect	Great Inequality	Holistic Model
Direction	Prograde ( $+19.5''/\text{yr}$ secular)	Ecliptic-retrograde ( $\sim -30.9''/\text{yr}$ )
Current ecliptic-retrograde	Transient ( $\sim 900$ -yr phase)	Permanent feature
WebGeoCalc match ( $\sim -3,400''/\text{cy}$ )	Requires large GI amplitude in $\varpi$	$\sim -3,372''/\text{cy}$ (geocentric)
Saturn’s role	Same as other planets	Anti-phase pivot (Laws 3, 5, 6)
Testable prediction	Rate reverses within $\sim 450$ yr	Rate stays ecliptic-retrograde

The two theories make a decisive, testable prediction: over decades to centuries of continued high-precision ephemeris tracking, Saturn’s  $d\varpi/dt$  should either show curvature toward zero (Great Inequality) or remain steady near  $-3,100$  to  $-3,400''/\text{cy}$  (this model).

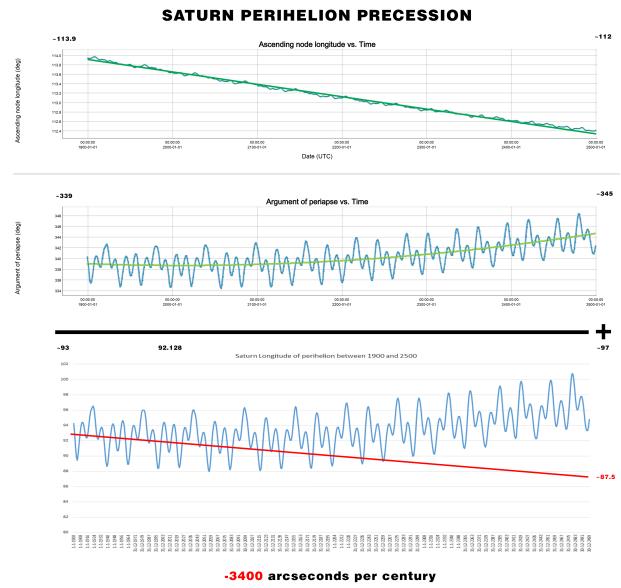


**Figure 6:** Saturn’s perihelion precession decomposed from JPL WebGeoCalc (1900–2500 AD). **Top:** Ascending node longitude ( $\Omega$ ) decreases smoothly (retrograde). **Middle:** Argument of periapee ( $\omega$ ) oscillates with the  $\sim 900$ -year Great Inequality. **Bottom:** Their sum  $\varpi = \Omega + \omega$  shows a net retrograde trend; the 1900–2000 slope is  $\sim -3,400''/\text{cy}$  (red line). The entire prograde-vs-retrograde debate concerns  $\omega$ : standard secular theory requires all  $g$ -eigenfrequencies to be positive (prograde), so any observed retrograde motion in  $\omega$  must be attributed to the Great Inequality. The model predicts  $\omega$  is permanently retrograde in the ecliptic frame.

### 6.2 The ICRF Perspective: A Fibonacci Chain

The model is formulated in the ecliptic frame — the natural frame for solar system dynamics. Secular perturbation theory, the Laplace-Lagrange eigensystem, and angular momentum conservation all operate in this plane; the planetary precession rates emerge from mutual gravitational interactions within it. The ICRF (International Celestial Reference Frame), fixed to distant quasars, provides an inertial reference, but no physical mechanism couples the solar system’s internal precession to that external frame. The ICRF rates are therefore a kinematic consequence of the ecliptic dynamics, not an independent constraint.

Nonetheless, viewing the same motions from the ICRF reveals a deeper Fibonacci structure. **In the ICRF, only Earth precesses prograde.** Earth’s ecliptic rate ( $H/16 \approx 61.840''/\text{yr}$ ) is the only one that exceeds the general precession of the equinoxes ( $H/13 \approx 50.245''/\text{yr}$ ). All other planets — including Jupiter — precess retrograde in the ICRF. The frame transformation subtracts the general precession uniformly:

$$\text{ICRF rate} = \text{ecliptic rate} - H/13 \quad (15)$$

The correction  $H/13$  (general precession = Earth’s axial precession period) is the same for all planets — it is a property of the reference frame, not the individual planet. The resulting ICRF identities are Fibonacci *subtraction* identities:

- **Earth:** ecliptic 16 – general precession 13 = ICRF +3 ( $16 - 13 = 3$ )

**Table 9:** Perihelion precession: ecliptic vs. ICRF frame (all planets). ICRF rate = ecliptic rate  $-H/13$ . Only the three Law 6 planets (bold) have pure Fibonacci ICRF denominators.

Planet	Ecliptic $H/n$	Period (yr)	Dir.	ICRF $H/n$	Period (yr)	Dir.
Mercury	$H \times (8/11)$	243,867	prograde	$-8H/93$	28,844	retrograde
<b>Venus</b>	<b><math>-8H/6</math></b>	<b>447,089</b>	<b>retrograde</b>	$-8H/110$	24,387	retrograde
<b>Earth</b>	<b><math>H/16</math></b>	<b><math>\sim 20,957</math></b>	<b>prograde</b>	<b><math>+H/3</math></b>	<b><math>\sim 111,772</math></b>	<b>prograde</b>
Mars	$H \times (8/35)$	76,644	prograde	$-8H/69$	38,877	retrograde
<b>Jupiter</b>	<b><math>H/5</math></b>	<b>67,063</b>	<b>prograde</b>	<b><math>-H/8</math></b>	<b><math>\sim 41,915</math></b>	<b>retrograde</b>
<b>Saturn</b>	<b><math>-H/8</math></b>	<b><math>\sim 41,915</math></b>	<b>retrograde</b>	<b><math>-H/21</math></b>	<b>15,967</b>	<b>retrograde</b>
Uranus	$H/3$	$\sim 111,772$	prograde	$-H/10$	33,532	retrograde
Neptune	$2H$	670,634	prograde	$-2H/25$	26,825	retrograde

- **Jupiter:** ecliptic 5 – general precession 13 = ICRF  $-8$  ( $5 - 13 = -8$ )
- **Saturn:** ecliptic  $-8$  – general precession 13 = ICRF  $-21$  ( $-8 - 13 = -21$ )

These follow directly from the Fibonacci recurrence: since  $5 + 8 = 13$ , subtracting 13 from 5 gives  $-8$ ; since  $8 + 13 = 21$ , subtracting 13 from  $-8$  gives  $-21$ ; since  $3 + 13 = 16$ , subtracting 13 from 16 gives 3. The complete Fibonacci chain  $3 \rightarrow 5 \rightarrow 8 \rightarrow 13 \rightarrow 21$  is still generated — but by subtraction of the general precession, not by addition.

**Earth is the sole prograde planet in the ICRF** — an exception created by the Fibonacci number  $H/13$  (the general precession). Only the three Law 6 planets (Earth, Jupiter, Saturn) have pure Fibonacci ICRF denominators; other planets have non-Fibonacci ICRF denominators, consistent with Jupiter and Saturn carrying  $\sim 85\%$  of the solar system’s angular momentum.

### 6.2.1 Reference Frame Duality

Earth is the sole planet whose ecliptic apsidal rate ( $16/H$ ) exceeds the general precession rate ( $13/H$ ). This creates a *reference frame duality*: Earth’s perihelion direction precesses prograde in both frames, and its ICRF perihelion rate remains prograde ( $+H/3 = \sim 111,772$  yr), making it the only planet whose inclination oscillation is driven by a prograde ICRF perihelion (Fig. 3c). For all other planets, the ICRF perihelion rate is retrograde.

The divisor 5 in Table 1 corresponds to the *Ecliptic Precession*: the rate at which Earth’s orbital plane precesses around the invariable plane. This matches the Laskar  $s_3$  eigenfrequency (68,750 yr, 2.9% difference; Laskar et al. 2004), independently confirming the identification.

Alongside the subtraction identities above, the ICRF denominators also satisfy Fibonacci *addition* identities:

- Earth ICRF apsidal (3) + Ecliptic Precession (5) = Jupiter ICRF (8)
- Ecliptic Precession (5) + Jupiter ICRF (8) = general precession (13)
- Jupiter ICRF (8) + general precession (13) = Saturn ICRF (21)

The complete Fibonacci chain  $3 \rightarrow 5 \rightarrow 8 \rightarrow 13 \rightarrow 21$  thus appears twice: once through subtraction of general precession from ecliptic rates, and once through addition across ICRF rates. The Ecliptic Precession ( $H/5$ ) serves as the bridge between the two frames.

### 6.3 Extending the Framework to All Planets

The Fibonacci framework extends beyond perihelion precession to axial precession and obliquity cycles for all planets.

Each planet’s axial precession period can be expressed in terms of  $H$  (Table 10).

**Table 10:** Axial precession periods expressed in  $H$

Planet	$H$ expression	Period	Dir.	Observed / Theory	Source
Mercury	$8H/9$	298,060 yr	retro	$\sim 300$ kyr (Cassini)	Peale 2006
Venus	$8H/91$	29,478 yr	pro	$\sim 29$ kyr	Cottureau & Souchay 2009
Earth	$H/13$	25,794 yr	retro	$\sim 25,772$ yr	Capitaine et al. 2003
Mars	$H/2 = 8H/16$	167,659 yr	retro	170,400 yr	Konopliv et al. 2021
Jupiter	$8H/21$	127,740 yr	retro	113–136 kyr	Saillenfest et al. 2020
Saturn	$4H/3 = 8H/6$	447,089 yr	retro	400–480 kyr	Saillenfest et al. 2021
Uranus	$H \times 610$	$\sim 204$ Myr	pro	$\sim 40$ – $50$ Myr	Saillenfest et al. 2022
Neptune	$H \times 68$	$\sim 22.8$ Myr	retro	$\sim 70$ Myr (est.)	Rogoszinski & Hamilton 2020

Mercury’s  $8H/9$  coincides with its ascending-node period (Cassini state, confirmed by MESSENGER). Jupiter’s  $8H/21$  uses  $F_6/F_8 = 8/21$ , a clean Fibonacci ratio. Mars ( $H/2 = 8H/16$ ) matches the InSight measurement to 1.7%. Uranus and Neptune have extremely slow axial precession ( $\sim 40$ – $200$  Myr), with large observational uncertainties.

**Obliquity cycles.** The Fibonacci decomposition that produces Earth’s obliquity cycle ( $H/8$  from the identity  $3+5 = 8$ ) extends to all planets where the perihelion ecliptic rate numerator can be Fibonacci-decomposed. Three obliquity cycles are confirmed by observation; three remain as testable predictions:

**Table 11:** Obliquity cycle predictions

Planet	Predicted	Observed / Theory	Status	Source
Mercury	$8H/3 = 894,179$ yr	$\sim 895,000$ yr	0.2%	Bills 2005
Earth	$H/8 = \sim 41,915$ yr	$\sim 41,040$ yr	2%	Laskar 1993
Mars	$8H/21 = 127,740$ yr	$\sim 124,800$ yr	2.4%	Laskar et al. 2004
Jupiter	$H/2 = 167,659$ yr	no regular cycle	prediction	Saillenfest et al. 2020
Saturn	$H/3 = 111,772$ yr	no regular cycle	prediction	Saillenfest et al. 2021
Uranus	$H/2 = 167,659$ yr	frozen at $\sim 98^\circ$	prediction	Saillenfest et al. 2022

Venus and Neptune have obliquity cycle = |ICRF perihelion period| (auto-derived from their ecliptic periods; tidally damped). In the two-component formula, the inclination and obliquity terms are at the same frequency and cancel exactly, producing constant obliquity — consistent with observations (Venus tidally damped at  $177^\circ$ , Neptune frozen at  $\sim 28^\circ$ ).

**Universal two-component formula.** Every planet with an obliquity cycle follows the same two-component structure as Earth (Eq. 19), with one cosine term at the ICRF perihelion period (inclination component) and one at the obliquity cycle period (obliquity component), both with amplitude  $A_p = \psi / (d_p \times \sqrt{m_p})$  from Law 2:

$$\begin{aligned} \varepsilon_p(t) = & \varepsilon_{p,J2000} \\ & - A_p [\cos(\omega_i t) - \cos(\omega_i t_{2000})] \\ & + A_p [\cos(\omega_o t) - \cos(\omega_o t_{2000})] \end{aligned} \quad (16)$$

where  $\omega_i = 2\pi/T_{\text{ICRF}}$  and  $\omega_o = 2\pi/T_{\text{obliq}}$ . The anchoring offsets ensure  $\varepsilon_p(2000) = \varepsilon_{p,J2000}$  exactly.

**Mean obliquity.** The time-averaged obliquity over the Solar System Resonance Cycle ( $8H$ ) differs from the J2000 snapshot because the cosine terms average to zero, leaving only the constant anchoring offsets:

$$\bar{\varepsilon}_p = \varepsilon_{p,J2000} + A_p \cos(\omega_i t_{2000}) - A_p \cos(\omega_o t_{2000}) \quad (17)$$

**Table 12:** Mean obliquity (analytical, averaged over  $8H$ )

Planet	J2000 (°)	Mean (°)	Shift (°)
Mercury	0.03	0.01	-0.02
Venus	2.64	2.64	—
Earth	23.44	23.41354	-0.03
Mars	25.19	25.40	+0.21
Jupiter	3.13	3.12	-0.01
Saturn	26.73	26.80	+0.07
Uranus	82.23	82.24	+0.01
Neptune	28.32	28.32	—

**Formula midpoint stability.** The formula midpoint (around which the two-cosine oscillation is centered) remains close to the J2000 snapshot for each planet, typically within  $\pm 0.2^\circ$ . Mars’s midpoint ( $25.40^\circ$  vs J2000  $25.19^\circ$ ) differs by only  $0.21^\circ$ . Mercury, Jupiter, Saturn, and Uranus all have midpoints within  $0.1^\circ$  of their J2000 values. This stability reflects that the inclination-amplitude oscillation is small relative to the mean obliquity for most planets.

Cross-planet connections emerge: Mars’s obliquity cycle equals Jupiter’s axial precession ( $8H/21$ , where  $21 = F_8$ ), and Earth’s obliquity cycle equals both Saturn’s ecliptic perihelion period and Jupiter’s ICRF perihelion period ( $H/8$ ).

**Eccentricity cycles.** Each planet’s eccentricity cycle is the meeting frequency of its axial precession and its perihelion precession in the ICRF — the same derivation that produces Earth’s  $H/16$  cycle (Table 13).

**Table 13:** Eccentricity cycles from axial–perihelion meeting frequencies

Planet	Axial dir.	Peri ICRF dir.	$H$ expression	Period
Mercury	retro	retro	$2H/21$	31,935 yr
Venus	pro	retro	$8H/19$	141,186 yr
<b>Earth</b>	<b>retro</b>	<b>pro</b>	<b><math>H/16</math></b>	<b><math>\sim 20,957</math> yr</b>
Mars	retro	retro	$8H/53$	50,614 yr
Jupiter	retro	retro	$8H/43$	62,385 yr
Saturn	retro	retro	$4H/81$	16,559 yr
Uranus	pro	retro	$\approx H/10$	33,532 yr
Neptune	retro	retro	$\approx 2H/25$	26,825 yr

When axial and perihelion ICRF precessions move in opposite directions (Earth, Venus, Uranus), their rates add; when in the same direction, the rates subtract. For Uranus and Neptune, the extremely slow axial precession ( $\sim 40$ – $200$  Myr) makes their eccentricity cycle approximately equal to the perihelion ICRF period.

#### 6.4 Ascending Node Periods: Integer Divisors of $8H$

Each planet’s ascending node regression period takes the form  $T_\Omega = 8H/N$  for an integer  $N$ . The eight integers are jointly fit to the JPL J2000-fixed-frame ascending-node trends, with Jupiter and Saturn locked to a shared  $N = 36$  to keep the gas-giant pair from drifting apart in the long-term integration.

Across all 7 fitted planets, the  $8H/N$  integers reproduce JPL’s J2000-fixed-frame ascending-node trends with a cumulative residual error of  $\sim 5.8''/\text{century}$  ( $\approx 0.8''/\text{century}$  per planet). The structural claim is that each planet’s ascending-node period is an integer divisor of a single Earth Fundamen-

**Table 14:** Ascending node periods as integer divisors of  $8H$ 

Planet	Period	Note
Mercury	$-8H/9$	
Venus	$-8H/1$	full Solar System Resonance Cycle
Earth	$-H/5 = -8H/40$	ecliptic precession (special)
Mars	$-8H/63$	
Jupiter	$-8H/36$	locked with Saturn
Saturn	$-8H/36$	locked with Jupiter
Uranus	$-8H/12$	
Neptune	$-8H/3$	

tal Cycle-derived super-period  $8H$  — all seven periods derive from one constant, rather than from seven independent measurements.

**Earth as a special case.** Earth’s ascending node period of  $-H/5 = -8H/40 = \sim 67,063$  years is the ecliptic precession rate and reflects its unique structural role as the planet defining the ecliptic frame. The negative sign indicates retrograde precession on the invariable plane. The ecliptic precession rate  $H/5$  is itself a derived quantity from the general precession ( $H/13$ ) and the obliquity cycle ( $H/8$ ):  $1/(H/13) - 1/(H/8) = 1/(H/5)$  closes the Fibonacci identity  $13 - 8 = 5$ , embedding Earth’s ascending node into the same Fibonacci hierarchy.

**Jupiter–Saturn lockstep.** Jupiter and Saturn share the same integer  $N = 36$ . Allowing them to drift independently makes the gas-giant pair separate in the long-term integration, breaking the resonance loop of Law 6; the shared  $N$  is therefore a structural constraint of the joint model, not a coincidence.

**Observability limitation.** These ascending node periods describe motion over 50,000–2,000,000 year timescales. With only  $\sim 4,000$  years of recorded astronomy, the periods cannot be observationally verified by direct observation of a complete cycle. The model’s contribution is the structural derivation: all seven periods derive from a single constant ( $H$ ) and a single super-period ( $8H$ ).

## 7. Physical Origin: Formation-Epoch Freezing

KAM theory (Section 2) explains why Fibonacci ratios are *preferred*. This section presents evidence that the observed precision — 99.9975% inclination balance (Law 3) and 99.8632% eccentricity balance (Law 5), computed from J2000 orbital elements and phase-derived base eccentricities — originates from the solar system’s formation epoch.

### 7.1 The Three-Phase Mechanism

**Phase 1 — Protoplanetary disk (0–10 Myr):** Planets form and migrate within a gas disk. Dissipative forces — gas drag, disk torques, tidal interactions — continuously push orbits toward configurations that minimize the Angular Momentum Deficit (AMD), the conserved quantity governing long-term stability (Laskar, 1997).

**Phase 2 — KAM selection:** Among all AMD-minimizing configurations, those organized by Fibonacci ratios have the widest stability margins (KAM theory). Dissipative evolution therefore preferentially *converges toward Fibonacci-organized configurations* — not because Fibonacci is imposed, but because Fibonacci configurations are the deepest

stability wells in the energy landscape.

**Phase 3 — Disk dissipation (~3–10 Myr):** When the gas disk dissipates, the dissipative mechanism shuts off. The Fibonacci configuration is *frozen* — like a ball settling into the deepest valley and then the landscape hardening around it. 4.5 billion years of conservative Hamiltonian dynamics have preserved the architecture because KAM tori protect it against perturbation.

## 7.2 Hierarchy of Certainty

Not all claims carry equal evidence:

**Table 15:** Hierarchy of certainty

Claim	Evidence	Status
Fibonacci structure in orbital architecture	$p \leq 1.5 \times 10^{-4}$ ( $\approx 3.62\sigma$ )	Established
Structure acts on AMD-natural variables	0.11% vs > 28% spread	Established
KAM provides mathematical foundation	Proven theorem	Established
Structure frozen at formation	$N$ -body: no mode preserves it	Well-supported

The *existence* of non-trivial Fibonacci structure beyond chance is supported at  $3.62$ – $4.75\sigma$  (direct joint permutation test on the 4 empirical tests, then Monte Carlo joint tests over 9 tests — model-independent, no distributional assumptions; see Section 8). The *mechanism* — KAM theory selecting golden-ratio-compatible orbits, frozen at formation — is well-supported. The *specific values* ( $H = 335, 317, \psi, K$ ) are empirically determined and not yet derived from first principles.

## 7.3 Three Fibonacci Levels

The Fibonacci structure operates at three distinct, nested levels — each independently observable. This is not a single accidental pattern but a hierarchy of nested Fibonacci relationships:

**Level 1 — Fibonacci  $d$ -values (Laws 2–5):** Each planet is assigned a Fibonacci number  $d \in \{3, 5, 21, 34\}$  that determines its inclination amplitude through  $A = \psi/(d \times \sqrt{m})$ . The eight  $d$ -values form mirror-symmetric pairs across the asteroid belt: Mercury–Uranus ( $F_8 = 21$ ), Venus–Neptune ( $F_9 = 34$ ), Mars–Jupiter ( $F_5 = 5$ ), Earth–Saturn ( $F_4 = 3$ ). This level determines the *scalar balance* (Laws 3 and 5) — the genuine constraint that, together with mirror symmetry, selects the unique configuration out of 7,558,272 tested (Section 4.5).

**Level 2 — ICRF perihelion periods are  $H$ /Fibonacci (Law 1):** Earth’s major precession periods divide the Earth Fundamental Cycle by Fibonacci numbers:  $H/3, H/5, H/8, H/13, H/16$ . The Fibonacci addition rule applies as a beat frequency identity:  $1/T_n + 1/T_{n+1} = 1/T_{n+2}$ . The Saturn–Jupiter–Earth resonance triangle (Law 6) is a direct consequence:  $1/(H/3) + 1/(H/5) = 1/(H/8)$ .

**Level 3 — Ascending-node periods are  $8H/N$ :** The ascending node regression rates are integer divisors of the Solar System Resonance Cycle ( $8H$ ), with Jupiter and Saturn locked to a shared  $N = 36$ . Across all 7 fitted planets, the  $8H/N$  integers reproduce JPL’s J2000-fixed-frame ascending-node trends with a cumulative residual error of  $\sim 5.8''/\text{century}$  ( $\approx 0.8''/\text{century}$  per planet, Section 6.4). The structural claim is that these periods are  $H$ -derived integer divisors of the Solar System Resonance Cycle.

The three levels are nested:  $d$ -values (Level 1) determine the amplitudes,  $H$ /Fibonacci periods (Level 2) determine

the dominant precession rates, and  $8H/N$  eigenfrequencies (Level 3) determine the secular ascending node motion. Each level is independently observable, and each agrees with measurement.

## 8. Statistical Significance and Exoplanet Evidence

### 8.1 11 Tests, Three Null Distributions

To address concerns first raised by Backus (1969) about Fibonacci structure in planetary systems, a comprehensive significance analysis was performed using 11 test statistics covering all 6 laws plus four findings. Each was evaluated against three independent null distributions:

- **Permutation** (exhaustive  $8! = 40,320$  trials): same values, randomly reassigned to planets.
- **Log-uniform Monte Carlo** ( $10^6$  trials): random eccentricities and amplitudes from physical ranges, random  $d$ -values from Fibonacci sets, random period denominators, random year-length ratios.
- **Uniform Monte Carlo** ( $10^6$  trials): same ranges, flat distribution.

Of the 11 tests, 4 are genuinely *empirical* under the permutation null (Laws 3, 5; Findings 4 and 6) and 9 are combinable under the Monte Carlo nulls (the empirical set plus Laws 1, 6; Findings 1, 1b; year-length beat, which become meaningful when the null draws random  $d$ -assignments, random period denominators, and random year lengths). Two tests (Laws 2 and 4) remain excluded under all nulls:

- **Multiset-invariant under permutation** — Law 1 (Fibonacci denominators), Law 6 (E–J–S resonance), Finding 1 (mirror symmetry), Finding 1b (d-set Fibonacci clustering), Year-length beat. Permutation cannot disturb the multiset of values or a single scalar; but Monte Carlo can, so these are included in the MC joint test.
- **Tautological by construction** — Laws 2 ( $\psi$  full) and 4 ( $K$  amplitude). The model defines  $\text{INCL\_AMP}_p \equiv \psi/(d_p \sqrt{m_p})$  and  $\text{ECC\_AMPLITUDE}_p \equiv K \sin(\varepsilon_p) \sqrt{d_p}/(\sqrt{m_p} a_p^{3/2})$ , so both relations hold *identically*, not approximately. Empirical testing of these laws would require independent observed amplitudes for multi-millennial planetary oscillations — and no such observations exist on human timescales. Even Laskar’s secular theory amplitudes are themselves  $N$ -body simulation outputs, not measurements; comparing one theoretical fit against another does not constitute an independent statistical test. These laws are therefore reported as internal-consistency checks but cannot contribute to combined significance under any null.

The 4 empirical tests are not statistically independent — all four use the same fundamental quantity  $v_j = \sqrt{m_j} a_j^{3/2} e_j / \sqrt{d_j}$  — so older combining methods (Fisher’s, Stouffer’s+Brown) must absorb a correlation penalty. The direct joint test used here avoids the approximation by computing the combined statistic’s null distribution directly (Table 16).

**Headline statistic: direct joint permutation test.** The headline is a direct joint permutation test over the 4 empirical tests. Each test’s raw statistic is studentized against the

null mean and standard deviation computed across all 8! permutations; the four studentized  $z$ -scores are summed into a single combined statistic  $T = \sum_i z_i$ ; and the  $p$ -value is the fraction of null permutations with  $T_{\text{null}} \geq T_{\text{obs}}$ .

This approach is model-independent (no Gaussian or  $\chi^2$  assumption), self-correcting for correlation (because the joint null is computed from the same shared permutation that generates the correlation, no explicit variance-inflation factor is needed — the correlation is baked into the null by construction), and has no floor-clamp artifact ( $p \geq 1/(n+1)$  by construction). For reference, the *measured* average pairwise correlation between the four tests under the permutation null is  $\bar{r} = 0.283$  (replacing an earlier estimate of  $\bar{r} \approx 0.5$  that proved too conservative). Under the MC nulls the measured correlation is much smaller ( $\bar{r} \approx 0.032$ ) because random  $d$ -assignments break the shared  $v_j$  dependency.

All 4 empirical tests reach  $p < 0.01$  in the permutation null, and all 9 MC-combinable tests reach  $p < 0.05$  in both Monte Carlo nulls. The joint combined  $p$ -value is robust across the three null distributions and lands in a tight range:

$$\begin{aligned} p_{\text{joint, perm.}} &= 1.5 \times 10^{-4} && \approx 3.62 \sigma \\ p_{\text{joint, log-u. MC}} &= 1.0 \times 10^{-6} && \approx 4.75 \sigma \\ p_{\text{joint, unif. MC}} &= 1.0 \times 10^{-6} && \approx 4.75 \sigma. \end{aligned} \quad (18)$$

The permutation result ( $\approx 3.62 \sigma$ ) is the most defensive figure — it conditions on the actual values and tests only the planet-to-value assignment, making no assumptions about what counts as a “random” planetary system. The Monte Carlo nulls test the more general question of whether fully randomised systems would reproduce the patterns, and give a stronger answer ( $\approx 4.75 \sigma$ ). The two MC nulls agree to within  $0.01 \sigma$ , indicating complete insensitivity to the choice between log-uniform and uniform sampling. The headline comfortably exceeds the conventional  $3\sigma$  “evidence” threshold across all three null distributions, and the MC results lie just below the particle-physics  $5\sigma$  “discovery” threshold ( $p \approx 3 \times 10^{-7}$ ).

**Jackknife: robustness to dropping any single planet.** A leave-one-out jackknife re-runs the direct joint permutation test (now over  $7! = 5,040$  permutations) with each planet removed from the system in turn (Table 17). This quantifies how much of the combined signal rides on any one body. Dropping Jupiter collapses the signal to  $\approx 0.5 \sigma$ , and dropping Uranus collapses it to  $\approx 0.9 \sigma$ .

This is required by the model’s structural claims: the  $v_j$  balance is *global* (each side of the Fibonacci  $d$ -ladder must contribute), so removing any high- $v$  planet destroys the balance. The pattern matches what the six laws predict — a cooperative structure in which all eight planets participate, with the outer planets (Jupiter, Saturn, Uranus, Neptune) carrying the largest  $v$ -weights. Reaching the full  $3.62 \sigma$  requires *all* eight planets; no individual planet alone drives the result.

**Comparison with supporting approximations.** Two older combining methods are retained for transparency but are approximations of the direct joint test:

- **Stouffer’s  $Z$  with measured  $\bar{r}$**  (permutation:  $1.8 \times 10^{-5}$ ,  $\approx 4.1 \sigma$ ). Converts each per-test  $p$ -value to a one-tailed

**Table 16:** Statistical significance of Fibonacci structure (11 tests)

Test	Observed	Perm.	Log-u.	Unif.
1. Law 1 Fib. denominators <sup>‡</sup>	7/8	1	2.6e-5	3.0e-5
2. Law 2 $\psi$ full <sup>§</sup>	0.0000%	1	1	1
3. <b>Law 3 Incl. balance</b>	<b>99.9975%</b>	<b>7.4e-3</b>	<b>1.0e-5</b>	<b>0.8e-5</b>
4. Law 4 $K$ amplitude <sup>§</sup>	0.0000%	1	1	1
5. <b>Law 5 Ecc. balance</b>	<b>99.8632%</b>	<b>7.2e-4</b>	<b>3.7e-4</b>	<b>3.7e-4</b>
6. Law 6 E–J–S reson. <sup>‡</sup>	exact	1	0.032	0.032
7. F1 Mirror symm. <sup>‡</sup>	4/4	1	1.2e-4	1.5e-4
8. F1b d-set clustering <sup>‡</sup>	yes	1	0.020	0.020
9. <b>F4 Saturn pred.</b>	<b>0.27%</b>	<b>7.2e-4</b>	<b>3.7e-4</b>	<b>3.7e-4</b>
10. <b>F6 Solo planet ID</b>	<b>0.27%</b>	<b>4.0e-3</b>	<b>2.8e-3</b>	<b>3.1e-3</b>
11. Year-length beat <sup>‡</sup>	0.0048%	1	$< 10^{-6}$	$< 10^{-6}$
<b>Joint permutation test (headline)</b>		<b><math>1.5 \times 10^{-4}</math></b>	<b><math>1.0 \times 10^{-6}</math></b>	<b><math>1.0 \times 10^{-6}</math></b>

<sup>‡</sup> **Structural / multiset-invariant** (Laws 1, 6; Findings 1, 1b; Year-length beat). Permutation yields  $p = 1$  by construction (the multiset of values is preserved under shuffling, or the observation is a single scalar). Under the Monte Carlo nulls the tests *are* meaningful — random  $d$ -assignments, random period denominators, and random year lengths produce distinct null distributions — and these five tests are therefore *included* in the MC joint combined statistic.

<sup>§</sup> **Tautological by construction** (Laws 2 and 4). The model defines amplitudes as  $\psi/(d\sqrt{m})$  and  $K \sin(\varepsilon) \sqrt{d}/(\sqrt{ma^3/2})$ , so the test relations hold identically under any null. Reported as internal-consistency checks; excluded from every combined statistic.

**Headline:** direct joint permutation test — studentized combined statistic  $T = \sum_i z_i$  over the  $k = 4$  empirical tests,  $p = \#\{T_{\text{null}} \geq T_{\text{obs}}\}/n$ . Under the MC nulls the joint test combines  $k = 9$  tests. Model-independent: no Gaussian assumption, no correlation-correction factor (the joint null captures the correlation directly).

**Table 17:** Leave-one-out jackknife of the direct joint permutation test

Planet dropped	Joint $p$	Sigma
Mercury	$3.2 \times 10^{-2}$	$\approx 1.85 \sigma$
Venus	$2.4 \times 10^{-3}$	$\approx 2.82 \sigma$
Earth	$3.4 \times 10^{-3}$	$\approx 2.71 \sigma$
Mars	$5.0 \times 10^{-3}$	$\approx 2.58 \sigma$
<b>Jupiter</b>	<b><math>3.1 \times 10^{-1}</math></b>	<b><math>\approx 0.49 \sigma</math></b>
Saturn <sup>†</sup>	$6.6 \times 10^{-2}$	$\approx 1.50 \sigma$
<b>Uranus</b>	<b><math>1.9 \times 10^{-1}</math></b>	<b><math>\approx 0.86 \sigma</math></b>
Neptune	$6.0 \times 10^{-2}$	$\approx 1.55 \sigma$
<b>Full 8-planet suite</b>	<b><math>1.5 \times 10^{-4}</math></b>	<b><math>3.62 \sigma</math></b>

<sup>†</sup> F4 undefined when Saturn is dropped;  $k = 3$  tests used.

$z$  and sums with a variance-inflation factor  $1 + (k - 1)\bar{r}$ . Uses the measured correlation  $\bar{r} = 0.283$  instead of the previously hard-coded value of 0.5.

- **Fisher’s method** (permutation:  $8.7 \times 10^{-8}$ ). Combines log- $p$ -values into a  $\chi^2$  statistic; highly sensitive to floor-clamping at small  $p$ -values. Reported as a cross-check only.

Both give stronger apparent significance than the direct joint test, because both rely on Gaussian/ $\chi^2$  distributional assumptions that the direct test avoids. The gap is a useful indicator of how much the approximations contribute versus the raw data.

## 8.2 Exoplanet Context: A Question for Future Work

Compact multi-planet exoplanet systems raise the question of whether Fibonacci period-ratio patterns appear more broadly. TRAPPIST-1 (Grimm et al., 2018) has 5 of 6 consecutive period ratios near Fibonacci fractions (83%); Kepler-90 has 5 of 7 (71%). These observations are consistent with prior findings that Fibonacci fractions cluster preferentially in orbital period distributions (Pletser, 2019; Aschwanden, 2018).

However, neither system can test the deeper Fibonacci Laws presented here. TRAPPIST-1 is a known mean-motion resonance chain, so Fibonacci-like period ratios are partly a by-product of resonance rather than an independent realization of the same mechanism. Its eccentricities span only  $\sim 0.002$ – $0.01$  (a factor-of-4 dynamic range, compared with the solar system's  $141\times$  range), leaving the inclination and eccentricity balance conditions (Laws 3 and 5) untestable. Kepler-90 has only two mass measurements, which precludes any  $\xi$ - or  $\eta$ -based test. The period-ratio observations in these systems are therefore suggestive rather than confirmatory — they motivate future work once more TTV-mass-measured exoplanet systems become available, but they are not used as support for any of the eleven significance tests above, which rest entirely on solar system data.

## Part II: Consequences for Earth

### 9. Observable Consequences for Earth

The six Fibonacci Laws produce specific, testable consequences for Earth's orbital dynamics. Each of Earth's known precession phenomena emerges from the model's two counter-rotating reference points.

#### 9.1 Obliquity

The model's key structural insight is that observed obliquity is the sum of two oscillating components with equal amplitude:

$$\varepsilon(t) = \bar{\varepsilon} - A \cos\left(\frac{2\pi t}{T_{\text{incl}}}\right) + A \cos\left(\frac{2\pi t}{T_{\text{obliq}}}\right) \quad (19)$$

where  $\bar{\varepsilon} = 23.41354^\circ$  (mean obliquity),  $A = 0.63603^\circ$  (amplitude),  $T_{\text{incl}} = H/3 = \sim 111,772$  years (inclination component), and  $T_{\text{obliq}} = H/8 = \sim 41,915$  years (obliquity component). The two cosine terms have opposite signs: the inclination component is subtracted while the obliquity component is added. Maximum obliquity occurs when both terms reach their respective extremes such that they add constructively; minimum occurs when they cancel. The dominant visible period is  $H/8 \approx \sim 41,915$  years, matching the observed Milankovitch obliquity cycle. Agreement with standard theory is excellent for  $\pm 10,000$  years; beyond this range, the model predicts bounded oscillation within  $22.21^\circ$ – $24.72^\circ$  while Laskar's polynomial extrapolation diverges (Fig. 7).

**Table 18:** Obliquity: model vs. standard theory

Year	Model	La2004 (Laskar et al., 2004)	Chapront et al. 2002	Diff.
2000 AD	23.4393°	23.4393°	—	0
10,000 BC	24.5293°	24.1592°	24.3053°	$\sim 0.37^\circ$
10,000 AD	22.6182°	22.6534°	22.6370°	$\sim 0.04^\circ$

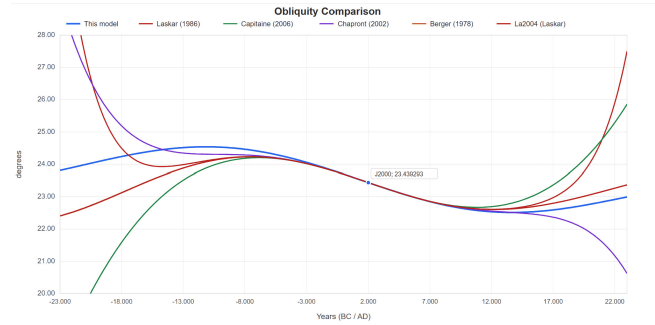


**Figure 7:** Obliquity predictions compared: this model (blue) versus La2004 (Laskar et al., 2004) (red) and Chapront et al. (2002) (green). Chapront's polynomial extrapolation diverges to unphysical values ( $20^\circ$ – $28^\circ$ ), while the model predicts bounded oscillation within  $22.21^\circ$ – $24.72^\circ$ .

**Independent amplitude confirmation.** Berger (1978) decomposed obliquity into 47 Fourier terms. The dominant term (frequency  $s_3 + k$ , period  $\sim 41,000$  years) has amplitude  $0.684^\circ$  — within 8% of the model's  $0.636^\circ$ . Physically,  $s_3$  is the eigenmode most strongly associated with Earth's orbital plane (precessing retrograde) and  $k$  is the axial precession rate (prograde); their beat  $s_3 + k$  produces the  $\sim 41,915$ -yr obliquity cycle, matching the model's Fibonacci beat ( $H/5$  ecliptic precession +  $H/3$  inclination precession  $\rightarrow H/8$  obliquity cycle, via  $3 + 5 = 8$ ). The secondary Fourier terms partially cancel the dominant term, which may account for the 8% gap.

**Why equal amplitudes?** The model's claim that both obliquity components oscillate by the same amplitude is not merely a simplification. In coupled oscillator theory, two effectively identical oscillators produce normal modes with exactly equal amplitudes. Angular momentum conservation (Noether's theorem) requires that two counter-rotating motions with equal amplitudes produce zero net angular momentum transfer — the symmetric, energy-conserving state. Unequal amplitudes would require explaining why the symmetry is broken.

The model's inclination precession cycle ( $\sim 111,772$  years) is independently validated by comparison with the La2010a numerical orbital solution (Laskar et al., 2011), which provides Earth's orbital elements in the invariable plane frame over 250 Myr (Fig. 8). Over 500 kyr, both show oscillation between  $\sim 0.5^\circ$  and  $\sim 2.9^\circ$ , with the current value near  $1.58^\circ$  (J2000; Souami & Souchay 2012).

#### 9.2 Eccentricity: The $\sim 20,957$ -Year Cycle

In contrast to Milankovitch's  $\sim 95,000/125,000/400,000$ -year eccentricity cycles, the model proposes a single  $\sim 20,957$ -year cycle. As the two reference points orbit in opposite directions, the effective distance between them oscillates with their meeting frequency. Current eccentricity: 0.01671022 (J2000). Base eccentricity: 0.015386. Amplitude:  $\pm 0.001356$ . Range: 0.0140–0.0167. Next minimum:  $\sim 11,725$  AD (Fig. 9).

Note: this eccentricity curve reflects only Earth's own  $\sim 20,957$ -year perihelion cycle. Saturn's eccentricity is predicted by Law 5, and the two are coupled through the balance system and Saturn's precession formula. Saturn's own

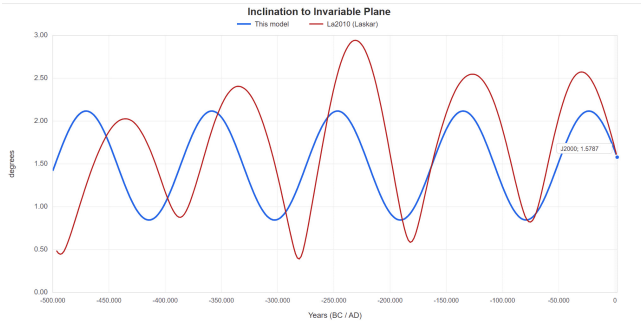


**Figure 8:** Orbital inclination compared: this model (blue) versus La2010a (Laskar et al., 2011) (red). Both show oscillation between  $\sim 0.5^\circ$  and  $\sim 2.9^\circ$  with the  $\sim 111,772$ -year period.

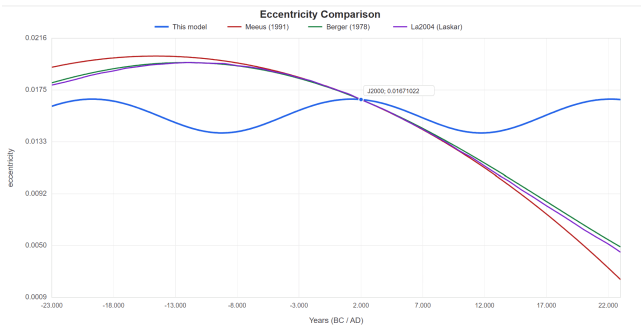


**Figure 9:** Eccentricity predictions: this model (purple) versus polynomials from Newcomb (1898) (blue), Harkness (1891) (red), and Meeus (1998) (green). Standard theory predicts decrease toward  $\sim 0.01$ ; the model predicts bounded oscillation with minimum at  $\sim 11,725$  AD.

ecliptic-retrograde precession ( $-H/8$ ) drives additional eccentricity changes that feed back into Earth — an effect not yet incorporated into the curve above.

### 9.3 Longitude of Perihelion

The longitude of perihelion advances through all  $360^\circ$  once per  $\sim 20,957$ -year cycle, currently at  $102.947^\circ$  (J2000). Comparison with Meeus (1998) shows close agreement for  $\pm 3,000$  years ( $\pm 0.025^\circ$  at 1000 AD,  $\pm 0.100^\circ$  at 2500 AD); beyond this range the predictions diverge (Fig. 10).

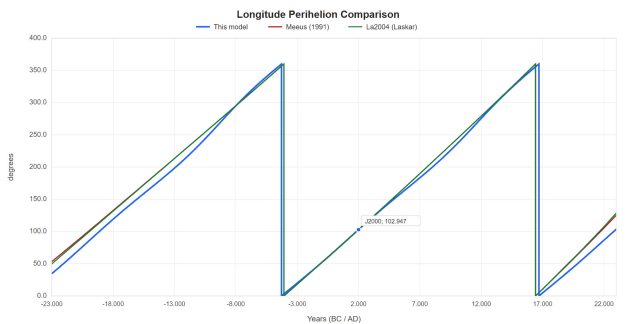


**Figure 10:** Longitude of perihelion: this model (blue) versus Meeus (1998) polynomial (red). Close agreement for  $\pm 3,000$  years around J2000.

### 9.4 Length of Day and Timekeeping

Standard theory attributes Earth’s rotational slowing to lunar tidal friction ( $\sim 2.3$  ms/century), predicting monotonic in-

crease in LOD. The model proposes an additional millennial-scale variation superimposed on tidal slowing (Table 19): LOD will slightly increase until  $\sim 6,000$  AD, then decrease until  $\sim 23,000$  AD. Short-term fluctuations are superimposed on this long-term trend. Earth unexpectedly began rotating faster in 2020, with the shortest day ever recorded on June 29, 2022 (1.59 ms under 24 hours) — qualitatively consistent with the model’s prediction that LOD varies cyclically.

**Table 19:** Length of Day: current vs. mean values

Parameter	Current value	Mean value
Solar day	$\sim 86,400.0001$ s	86,399.999677 s
Sidereal day	$\sim 86,164.090532$ s	86,164.0902196 s

Mitchell & Kirscher (2023) demonstrated that Earth’s day length stalled at approximately 19 hours for roughly 1 billion years during the mid-Proterozoic, likely due to atmospheric thermal tides balancing lunar tidal deceleration. This proves that LOD dynamics are more complex than simple tidal deceleration and that additional mechanisms can influence Earth’s rotation over geological timescales.

### 9.5 Obliquity & Eccentricity Define Lengths of Days & Years

Year lengths in days and the length of day in SI seconds follow closed-form Fourier harmonic series anchored to a single input constant ( $\bar{Y}_{\text{trop}} = 365.2422$  days). All three year types share the same form:

$$Y(t) = \bar{Y} + \sum_i \left[ s_i \sin\left(\frac{2\pi t}{T_i}\right) + c_i \cos\left(\frac{2\pi t}{T_i}\right) \right] \quad (20)$$

with periods  $T_i = H/n$  at small integer divisors  $n$ . The tropical year uses 12 harmonics (dominant:  $n = 8$ , the obliquity cycle), the sidereal year uses 5 (dominant:  $n = 8$  and  $n = 3$ ), and the anomalistic year uses 8 (dominant:  $n = 24$ , the beat between obliquity and inclination). The means are derived:  $\bar{Y}_{\text{trop}}$  from input rounding to  $H/16$ , then  $\bar{Y}_{\text{sid}} = \bar{Y}_{\text{trop}} \times (H/13)/(H/13 - 1)$  and  $\bar{Y}_{\text{anom}} = \bar{Y}_{\text{trop}} \times (H/16)/(H/16 - 1)$ . **Length of Day** follows from the sidereal year being fixed at 31,558,149.76 seconds:

$$D = \frac{31,558,149.76}{Y_{\text{sid}}(\text{days})} \quad (21)$$

The harmonic system reproduces the model’s year-length output to RMS  $\sim 0.03$  seconds on the tropical year and machine precision on the sidereal and anomalistic years.

The two formulas reveal a clean separation of roles. The tropical year is almost entirely determined by the obliquity cycle ( $T = H/8 \approx \sim 41,915$  yr), while eccentricity has negligible effect. Conversely, the sidereal year in days is determined by eccentricity: the sidereal year *in seconds* is fixed at 31,558,149.76 s (Earth’s orbital period relative to fixed stars, preserved by Kepler’s third law), but changing eccentricity changes the day length, which changes how many days fit into that fixed number of seconds. The day length varies by  $\sim 0.7$  ms peak-to-peak over the  $\sim 20,957$ -year perihelion cycle. Additionally, tropical years measured at different cardinal points differ by up to  $\sim 91$  seconds due to eccentricity effects (from  $-46$  s at the summer solstice to  $+45$  s at the

winter solstice at the current epoch), with the pattern rotating through the seasons over the perihelion cycle.

### 9.6 The Coin Rotation Paradox

The model reveals structural relationships between different measures of days and years (Table 20).

**Table 20:** Types of days and years

Type	Reference	Duration
Solar day	Sun’s apparent position	~86,400 s
Sidereal day	Precessing equinox	~86,164.09 s
Stellar day	Fixed stars (ICRF)	~86,164.10 s
Solar year	Equinox to equinox	~365.2422 d
Sidereal year	Fixed stars	31,558,149.76 s
Anomalistic year	Perihelion to perihelion	~365.2596324 d

The difference between stellar and sidereal day, and between sidereal and solar year, are direct consequences of axial precession. The precession rate varies over the Earth Fundamental Cycle: the cycle-averaged mean period is ~25,794 years, while the current instantaneous period is ~25,771 years. Using mean values, each difference accumulates to exactly one fewer unit per cycle:

*Day level:*

$$9.12 \text{ ms/sid. day} \times 366.25 \text{ sid. days/yr} \times \sim 25,794 \text{ yr} \\ \approx 86,164 \text{ s} = 1 \text{ sidereal day} \quad (22)$$

*Year level:*

$$1,223.49 \text{ s/yr (mean solar-sidereal year diff.)} \\ \times \sim 25,794 \text{ yr} \approx 31,558,150 \text{ s} = 1 \text{ sidereal year} \quad (23)$$

The coin rotation paradox (a coin rolling around an identical coin makes 2 rotations, not 1) manifests at these two scales:

- **Daily:** 366.25 sidereal days = 365.25 solar days per year (one extra stellar rotation from orbital motion)
- **Yearly:** 25,793 sidereal years = ~25,794 solar years per axial precession cycle (one fewer sidereal year from the precession orbit)

This self-consistency check links the model’s precession period to its day/year length formulas.

### 9.7 Milankovitch Beat Frequency Structure

The five Milankovitch-type cycles — apsidal precession, nodal regression, obliquity, axial precession, and climatic precession — are not independent. Standard orbital mechanics derives two as beat frequencies of the others (Vervoort et al., 2022). The model’s identification of all five as  $H/n$ , with  $n \in \{3, 5, 8, 13, 16\}$ , reveals that these beat frequency relationships are Fibonacci identities:

**Table 21:** Milankovitch beat frequencies as Fibonacci arithmetic

Physical equation	Model form	Fibonacci
$f_{\text{obliquity}} = f_{\text{axial}} - f_{\text{nodal}}$	$8/H = 13/H - 5/H$	$13 - 5 = 8$
$f_{\text{climatic}} = f_{\text{axial}} + f_{\text{apsidal}}$	$16/H = 13/H + 3/H$	$13 + 3 = 16$
$f_{\text{apsidal}} = f_{\text{obliquity}} - f_{\text{nodal}}$	$3/H = 8/H - 5/H$	$8 - 5 = 3$
$f_{\text{nodal}} = f_{\text{axial}} - f_{\text{obliquity}}$	$5/H = 13/H - 8/H$	$13 - 8 = 5$

The Fibonacci subtraction property ( $F_n = F_{n+2} - F_{n+1}$ ) is exactly the condition needed for the physical beat equations to close within the  $H/n$  system. Non-Fibonacci indices would fail: if the indices were  $\{3, 7, 10, 14, 17\}$ , then  $14 - 7 \neq 10$  and the obliquity equation would not close. All five standard Milankovitch periods are reproduced to within 0.3–2.8% from a single constant  $H$ .

**Deep-time extension.** Fibonacci multiples of  $H$  match established geological cycles:  $3H = 1,005,951$  yr matches the  $g_1 - g_5$  eccentricity beat (~980,000 yr, ~2.6% difference), and  $13H = 4,359,121$  yr matches the secular resonance libration period (Boulila et al., 2020) (~4,500,000 yr, ~3.1%). The Fibonacci ladder thus extends from  $H/16 = \sim 20,957$  yr to  $13H = 4,359,121$  yr — a factor of 208 in timescale.

**Eigenfrequency convergence.** Multiple independent Laskar (Laskar et al., 2004) eigenfrequency combinations converge on the same  $H/n$  values.  $H/3 = \sim 111,772$  yr (Inclination Precession) matches three independent combinations: the total apsidal rate (~112,000 yr, 0.6%), the  $g_3 - g_1$  eccentricity beat (109,950 yr, 1.2%), and the  $|s_2 - s_3|$  inclination beat (109,851 yr, 1.3%).  $H/5 = \sim 67,063$  yr (Ecliptic Precession) matches the  $s_3$  eigenfrequency (68,750 yr, 2.9%), the rate at which Earth’s orbital plane precesses around the invariable plane (Section 6.2). This convergence is not required by any known theory.<sup>3</sup>

### 9.8 Solstice Right Ascension Oscillation

The model predicts that the Sun’s ICRF right ascension at maximum declination (June solstice) oscillates with a ~41,915-year period and ±11 minutes amplitude, peaking at exactly 6h in 1246 AD. The IAU 2006 precession framework (Capitaine et al., 2003) independently confirms the mechanism: because the general precession in right ascension  $m_A = p_A \cos(\varepsilon) - \chi_A$  depends on  $\cos(\varepsilon)$ , and obliquity oscillates with a ~41,040-year period, the RA advance itself oscillates with the same period. The estimated amplitude (~±10 minutes) matches the model’s ±11 minutes. This effect is implicit in standard precession equations but has never been separately highlighted as an observable prediction.

## 10. The 100,000-Year Problem: Inclination-Side Eigenmode Beats

### 10.1 The Inclination-Side Family of Eigenmode Beats

The model’s position on the dominant ~100,000-year periodicity in ice core records (Hays et al., 1976) has two layers. Empirically, the cycle belongs to the inclination-side family of eigenmode beats (a planet-pair orbital-plane coupling) rather than to direct eccentricity forcing. Multi-component OLS analysis of LR04 with all 26 integer divisors of  $8H =$

<sup>3</sup>The eigenmodes  $g_j$  and  $s_j$  are mathematical objects (eigenvalues of the Laplace–Lagrange secular perturbation matrix) accepted by both Berger 1978 and the Holistic model; their numerical values come from the planetary masses and semi-major axes. What differs between the two frameworks is the attribution of each eigenmode to a single planet. Berger’s convention labels  $g_5$  as “Jupiter,”  $g_2$  as “Venus,”  $g_3$  as “Earth,” etc. (the planet whose contribution dominates that mode). The Holistic model treats the eigenmodes as composite modes of the multi-planet system and reserves the per-planet  $8H/n$  period table (§6.2) for its planet-specific cycles — so Jupiter’s ecliptic perihelion sits at  $H/5 = 67.06$  kyr, Jupiter’s ICRF perihelion at  $H/8 = 41.91$  kyr, and Jupiter Axial at  $8H/21$ , none of which equal  $1/g_5$ .

2,682,536 yr (the 8H Orbital Forcing Formula, §10.4) identifies the empirical centroid at  $n = 25 = 107.3$  kyr — the **Mercury–Mars  $s_1 - s_4$  nodal beat**, a planet-pair orbital-plane coupling. Direct eccentricity attribution faces three specific empirical failure modes:

- **405-kyr absence:** Berger’s strongest predicted eccentricity beat ( $g_2 - g_5$ ,  $\sim 405$  kyr) is essentially absent in post-MPT LR04 with amplitude ratio 0.120 versus the 100-kyr peak.
- **No bispectral 95k+125k phase coupling:** Hinich-style bispectrum on LR04 gives bicoherence 0.507, below the null 95th percentile of 0.555 — replicating the bispectral evidence of Muller & MacDonald (1997b).
- **Wrong-family centroid:** the 107-kyr empirical centroid is a *nodal* (orbital-plane) beat, not the *apsidal* (eccentricity) beat at 95–99 kyr that direct eccentricity attribution predicts.

Theoretically, within this inclination-side family the model proposes that Earth’s intrinsic inclination precession ( $\sim 111,772$  yr =  $H/3$ ) produces a second obliquity component contributing alongside the Mercury–Mars planet-pair nodal beat. Three inclination precession cycles span one Earth Fundamental Cycle ( $3 \times \sim 111,772 = 335,317$ ), producing the three major glacial sub-cycles visible in Antarctic ice core data (Fig. 11). At the available data length ( $T \approx 1.2$  Myr) the Rayleigh resolution limit  $\Delta P \approx P^2/T \approx 10$  kyr at  $P = 110$  kyr renders 95 kyr, 100 kyr, 107 kyr, and 112 kyr spectrally collinear — so the model’s  $H/3$  remains a candidate within the family, but cannot be singled out from the Mercury–Mars planet-pair beat at this data length. The case for the broader inclination-side attribution rests on the three failure modes above, not on a sharper peak position.

## 10.2 Peer-Reviewed Support: Muller & MacDonald (1997)

Muller & MacDonald (1997b), published in PNAS, demonstrated three key findings: (1) the eccentricity spectrum shows split peaks at  $\sim 95$  ka and  $\sim 125$  ka while climate shows a *broad single peak* spanning  $\sim 80$ – $125$  ka, without the spectral split that eccentricity would produce; (2) eccentricity’s dominant  $\sim 400$  ka component is largely absent from climate records; (3) inclination provides a better spectral match including phase relationships (bispectrum). Crucially, Muller measured inclination relative to the *invariable plane* — effectively the ICRF — yielding a  $\sim 100,000$ -year signal. In the ecliptic frame the same oscillation appears at  $\sim 68,700$  yr. The reference frame duality identified in Section 6.2 explains this distinction: Earth’s inclination dynamics operate in the ICRF ( $H/3 = \sim 111,772$  yr), not the ecliptic frame ( $H/5 = \sim 67,063$  yr). Ridgwell et al. (1999) independently questioned whether the spectral signature is consistent with a Milankovitch (eccentricity) origin, finding similar discrepancies. Muller’s proposed mechanism (interplanetary dust) was rejected by the community; the *spectral-shape mismatch* between eccentricity’s split peak and the climate record’s broad single peak has not been definitively refuted and is independent of the exact peak position within the band.

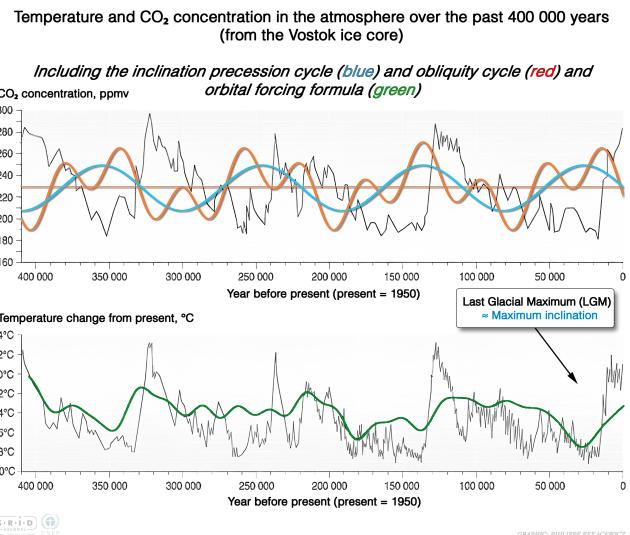


**Figure 11:** Vostok ice core temperature and CO<sub>2</sub> data with three overlaid curves: the model’s *theoretical* two-component obliquity decomposition on the CO<sub>2</sub> panel (top) —  $H/3 = \sim 111,772$  yr inclination precession (blue) and  $H/8 = \sim 41,915$  yr axial obliquity (red) — and the *empirical* 8H Orbital Forcing Formula (§10.4) on the temperature panel (bottom, green). The empirical curve’s 100-kyr-band amplitude is carried by the Mercury–Mars  $s_1 - s_4$  nodal beat at  $n = 25 = 107.3$  kyr (the empirical centroid), not by  $H/3$  at  $n = 24 = 111.77$  kyr (near-zero fitted amplitude on LR04). The visual alignment between the blue  $H/3$  curve and the glacial envelope reflects the model’s theoretical second-obliquity-component proposal, not an empirical identification of  $H/3$  as *the* climate signal. Background data from Petit et al. (1999), CC BY 4.0; model curves by the author.

## 10.3 Empirical Test: Spectral Analysis of Non-Tuned vs. Tuned Records

A common defence of the inclination interpretation appeals to circularity in ice core chronologies: many records employ orbital tuning — adjusting timescales to match Milankovitch insolation — which would artificially compress a true  $\sim 112$ -kyr signal toward  $\sim 100$  kyr. Modern chronologies (AICC2012; Veres et al. 2013) minimize this through annual layer counting, volcanic markers, and U-series dating (Kawamura et al., 2007), but for ice older than  $\sim 400$  ka, orbital tuning remains significant. We tested the chronology-bias hypothesis directly.

**Test design.** We compared the orbitally-tuned LR04 benthic  $\delta^{18}\text{O}$  stack (Lisiecki & Raymo, 2005) against the U-Th-dated speleothem record of Cheng et al. (2016). The Cheng2016 chronology is constructed independently of any orbital assumption (U-Th decay constants are atomic-physics-derived, with sub-1% precision across 0–640 kyr). If chronology bias were responsible for the  $\sim 10\%$  gap between  $\sim 100$  kyr and the model’s  $H/3 = \sim 111,772$  yr prediction, the non-tuned record should place the peak measurably closer to 112 kyr.

**Result.** Discrete Fourier transforms of both records on a 1.2-Myr window place the dominant peak in *the same FFT bin* ( $k = 6$ , centroid  $\approx 107$  kyr). A systematic  $\sim 10\%$  chronology offset between tuned and non-tuned records does *not* exist; the apparent gap to  $\sim 111,772$  yr is therefore not a dating

artifact.<sup>4</sup>

**Spectral resolution as the binding constraint.** At a record length  $T \approx 1.2$  Myr, the Rayleigh resolution limit at  $P = 110$  kyr is  $\Delta P \approx P^2/T \approx 10$  kyr. The candidates 95 kyr, 100 kyr, and 112 kyr therefore lie within one Rayleigh element of each other and are *spectrally collinear* — they cannot be independently determined by Fourier or multitaper methods at this data length. The model’s  $H/3 = \sim 111,772$  yr sits comfortably inside this resolution-limited band, alongside eccentricity’s 95-kyr / 125-kyr components. Both attributions are consistent with the data; what distinguishes them is the spectral *shape* (§10.2) and the missing 405-kyr eccentricity component, not the central peak position.

#### 10.4 The 8H Orbital Forcing Formula

Joint multi-component OLS fit on full LR04 ( $T = 5,320$  kyr) with the 26 integer divisors of  $8H$  identified as climate-active by the integer-divisor spectral scan yields an explicit predictive formula:

$$C(t) = c_0 + \sum_{n \in \mathcal{N}} \left[ a_n \cos\left(\frac{2\pi nt}{8H}\right) + b_n \sin\left(\frac{2\pi nt}{8H}\right) \right] \quad (24)$$

where  $t$  is age in kyr BP,  $C(t)$  is the normalised  $\delta^{18}\text{O}$  proxy, and  $\mathcal{N}$  is the set of 26 active integers. The fit achieves  $R^2 = 0.238$  with condition number 1.6 (all 26 components Rayleigh-resolvable at  $T = 5,320$  kyr); past-200-kyr local  $R^2 = 0.320$ . The three dominant components by amplitude are  $n = 65$  ( $k + s_3$  Earth obliquity at 41.27 kyr),  $n = 28$  ( $g_4 - g_5$  Mars–Jupiter eccentricity beat at 95.8 kyr), and  $n = 25$  (Mercury–Mars  $s_1 - s_4$  nodal at 107.3 kyr). Of the 26 integers, 25 carry clean physical interpretations as standard celestial-mechanics beats ( $k + g_j$  climatic precession,  $k + s_j$  obliquity sub-peaks,  $g_j - g_k$  eccentricity beats,  $s_j - s_k$  nodal beats) or as direct planet apsidal/nodal cycles from the model’s per-planet  $8H/n$  period table (§6.2); the remaining integer ( $n = 66$ ) reflects the arithmetic-mean cycle length of the non-stationary obliquity band rather than a distinct eigenmode beat.

**Per-planet observations.** Cross-referencing the 26 climate-active integers against the full per-planet  $8H/n$  period table reveals that Mars carries the cleanest direct fingerprint: two exclusive doc-55 direct matches in LR04 full (Mars apsidal at  $n = 35$ , Mars eccentricity cycle at  $n = 53$ ) plus three more in the pre-MPT window (Mars Axial  $n = 16$ , Mars Obliquity  $n = 21$ , Mars eccentricity confirmed at  $n = 53$ ). Mars’s apsidal eigenmode  $g_4 \approx 17.92''/\text{yr}$  lies within 3% of Earth’s  $g_3 \approx 17.37''/\text{yr}$  — a near-resonance that amplifies Mars’s gravitational coupling to Earth’s orbit despite Mars’s small mass. Neptune contributes no direct matches in LR04 full but appears in the pre-MPT spectrum via three eigenmode beats (Venus–Neptune  $g_2 - g_8$ , Earth–Uranus  $g_3 - g_7$ , Neptune–Earth  $s_8 - s_3$ ), visible only when post-MPT ice-sheet response does not dominate the spectrum.

<sup>4</sup>Full spectral analysis (Lomb–Scargle, multitaper, Hinich bispectrum, and multi-component OLS amplitude fits over LR04 and Cheng2016), together with the MPT amplitude-growth tests, is documented in the project’s technical docs (see Data Availability, docs/17-milankovitch-evidence).

**Forward projection.** Evaluating Eq. (24) at negative  $t$  identifies the Holocene as interglacial ( $C(0) = -0.638$  normalised); the next predicted natural glaciation peak sits at  $\sim 38,000$  yr from now ( $\sim 40,000$  AD), with the strongest glaciation in the next quarter-million years at  $\sim 194,500$  yr from now. Back-validation against the past 200 kyr places predicted glacial maxima at 29 kyr BP (vs. LGM  $\sim 20$  kyr BP, with the +9 kyr offset expected from ice-sheet response lag) and at 138 kyr BP (vs. MIS 6 at  $\sim 140$  kyr BP, within 2 kyr). The forward projection is consistent with the classical Berger & Loutre (2002) prediction ( $\sim 50$  kyr to next glaciation) within model uncertainty. Limitations: the formula captures only the orbital-forcing component ( $\sim 24\%$  of LR04 variance); ice-sheet hysteresis, carbon-cycle feedbacks, and anthropogenic  $\text{CO}_2$  are not modelled.<sup>5</sup>

#### 10.5 The Mid-Pleistocene Transition: Same Forcing, Different Response

The inclination-side eigenmode-beat structure (and Earth’s intrinsic  $H/3$  inclination precession at  $\sim 111,772$  yr) are *formation-epoch features* of the solar system (Section 7). Earth’s orbital inclination relative to the invariable plane was set when the protoplanetary disk dissipated  $\sim 4.5$  billion years ago. While long-term  $n$ -body integrations exhibit chaotic diffusion of orbital elements over  $\gtrsim 50$  Myr (Laskar, 1989), planetary eigenmodes are essentially stationary on Myr timescales — so the orbital forcing was effectively constant across the MPT. What changed was the climate system’s *sensitivity* to that forcing.

A windowed amplitude analysis across the MPT (pre-MPT 1,500–2,500 kyr BP versus post-MPT 0–1,000 kyr BP) gives concrete post/pre growth ratios per band: the 41-kyr obliquity peak actually *shrank* to  $\sim 0.72\times$  post-MPT, while the 100-kyr band grew  $\sim 1.64\times$ , the 23.7-kyr climatic-precession band grew  $\sim 2.19\times$ , and the 405-kyr eccentricity band shrank to  $\sim 0.34\times$ . The 41-kyr decrease is consistent with the standard “ice-sheet saturation silences the obliquity pacemaker” framing of Willeit et al. (2019): progressive  $\text{CO}_2$  decline and removal of easily-erodible regolith allowed ice sheets to grow past a critical size where they could survive obliquity maxima, shifting dominance from the 41-kyr-band response to the 100-kyr-band response.

A second candidate mechanism is **interplanetary dust concentration**: Farley (1995) confirmed an increase in extraterrestrial  $^3\text{He}$  flux beginning at  $\sim 1$  Ma, evidence that interplanetary dust accretion rose at the MPT. Muller & MacDonald (1997b) originally proposed that this dust modulates climate via the inclination of Earth’s orbital plane; the community rejected the specific dust–climate coupling mechanism, though Farley’s underlying dust-flux observation remains unchallenged. The dust mechanism is therefore listed as a candidate whose climate-driving role has not been confirmed.

Both candidate mechanisms are consistent with the model’s framework: the Fibonacci orbital architecture is a permanent feature of formation, while the MPT marks a change in climate sensitivity (not a change in the orbital forcing).

<sup>5</sup>Full empirical record, including methodology, per-test verdicts, and reproducibility scripts, is available at docs/17-milankovitch-evidence in the project repository.

ing itself). The post-MPT empirical signal in the 100-kyr band (Mercury–Mars  $s_1$ – $s_4$  nodal at 107 kyr) and the model’s theoretical  $H/3$  second-obliquity-component proposal both sit within the same inclination-side family.

## 11. Mercury’s Perihelion: A Reference Frame Consequence

### 11.1 Standard Framework and Alternative Interpretation

Mercury’s perihelion precesses at  $575.31 \pm 0.0015''/\text{cy}$  (ICRF) (Park et al., 2017). Newtonian perturbations account for  $\sim 532''/\text{cy}$ ; the remaining  $\sim 43''$  has been attributed to General Relativity since 1915. The model proposes this discrepancy arises from Earth’s reference frame motion rather than space-time curvature: Earth’s precession motions create a moving observation platform, and the model predicts this effect was  $\sim 43''$  around 1900 but is decreasing (Table 22).

**Table 22:** Mercury precession: model predictions over time

Year	Geocentric ( $''/\text{cy}$ )	ICRF ( $''/\text{cy}$ )	“Anomaly”
1800	$\sim 5,607.79$	$\sim 578.99$	$\sim 47.55''$
1900	$\sim 5,603.25$	$\sim 574.45$	$\sim 43.01''$
2000	$\sim 5,598.26$	$\sim 569.46$	$\sim 38.02''$
2100	$\sim 5,592.85$	$\sim 564.05$	$\sim 32.61''$

In the geocentric frame, the full Clemence (1947) breakdown (as reviewed by Berche & Medina 2024) shows Venus contributing  $\sim 278''/\text{cy}$  (52%), Jupiter  $\sim 154''/\text{cy}$  (29%), Earth  $\sim 90''/\text{cy}$  (17%), Saturn  $\sim 7''/\text{cy}$ , and Mars + others  $\sim 3''/\text{cy}$ , giving a Newtonian subtotal of  $5,557.18 \pm 0.85''/\text{cy}$  against an observed  $5,599.74 \pm 0.41''/\text{cy}$  — leaving a residual of  $42.56 \pm 0.94''/\text{cy}$ . The uncertainty on this residual ( $\sim 1''/\text{cy}$ ) is rarely emphasized.

The model does not claim GR is incorrect — GR has been confirmed independently across many other tests. For Mercury’s perihelion specifically, the model offers an alternative geometric interpretation that makes a different time-evolution prediction. Pitjeva & Pitjev (2013) show that solar system observations constrain but do not uniquely determine the relativistic contribution. The model implements Laplace–Lagrange secular theory, reproducing the standard Newtonian breakdown with  $\sim 96\%$  accuracy. A notable failure occurs for Venus: secular theory predicts  $1,075''/\text{cy}$  versus the observed  $204''/\text{cy}$ . This is a known limitation of first-order secular theory for low-eccentricity orbits — Venus’s nearly circular orbit ( $e = 0.007$ ) makes its perihelion direction extremely sensitive to perturbations. This connects to the finding (Section 12) that low-eccentricity planets’ precession fluctuations are dominated by Earth’s rate variations rather than geometric modulation — both observations reflect the same physics: perihelion is poorly defined for nearly circular orbits.

### 11.2 Independent N-Body Convergence

Three independent approaches converge at epoch J2000:

**Table 23:** Mercury geocentric precession: three independent sources

Source	Method	Total ( $''/\text{cy}$ )
Smulsky (2011)	Galactica N-body	5,601.9
Berche & Medina (2024)	Analytical (Clemence, 1947)	5,599.7
This model	Geometric framework	5,598.26

### 11.3 The Beat-Frequency Structure

The model predicts Mercury’s Earth-frame precession rate oscillates with a dominant period of  $\sim 7,451$  years (1/45 of the Earth Fundamental Cycle). The fluctuation ranges from  $-180''$  to  $+202''/\text{cy}$  around the  $\sim 531.4''$  baseline. When measured in the ecliptic frame, Mercury’s rate is constant at  $\sim 531.4''/\text{cy}$  — the fluctuation appears only in the Earth-frame measurement and averages to zero over the full Earth Fundamental Cycle.

### 11.4 The BepiColombo Test

MESSENGER measured  $575.31 \pm 0.0015''/\text{cy}$  at epoch  $\sim 2013$ . BepiColombo (orbit insertion November 2026, science operations from April 2027) will provide the second high-precision epoch (Table 24):

**Table 24:** BepiColombo prediction: model vs. GR

Theory	Value	Diff. from MESSENGER
<b>Model</b>	$\sim 574.61''/\text{cy}$	$-0.70''/\text{cy}$ ( $\sim 500\times$ unc.)
<b>GR</b>	$\sim 575.31''/\text{cy}$	constant (no change)

The model predicts the rate decreases by  $\sim 5.0''/\text{cy}$  per century ( $\sim 0.05''/\text{cy}$  per year). Over the  $\sim 14$  years between MESSENGER and BepiColombo, the predicted decrease of  $\sim 0.70''/\text{cy}$  is well within BepiColombo’s measurement precision — but only if BepiColombo’s analysis pipeline reports the raw measured perihelion advance, not a GR-inclusive ephemeris fit total (see Section 11.5). The Sun’s gravitational quadrupole moment ( $J_2$ ), which varies with solar activity (Mecheri & Abdelatif, 2022), creates an additional systematic uncertainty that BepiColombo will help resolve.

### 11.5 The Measurement Chain: An Open Question

The  $575''/\text{cy}$  value is reported as Mercury’s precession “relative to ICRF.” However, this is not a direct measurement. What is actually measured is the **geocentric** precession ( $\sim 5,604''/\text{cy}$ ), from which the Newtonian contribution ( $\sim 532''$ ) is subtracted to obtain the heliocentric rate, and the  $\sim 43''$  residual is attributed to GR. The measurement chain also depends critically on Earth’s position in ICRF, calculated from Earth orientation models that account for precession, nutation, and polar motion. If Earth’s long-period precession motions ( $\sim 25,794$  and  $\sim 111,772$  year cycles) have any systematic modeling errors, these would propagate into Mercury’s calculated position. The model proposes that the *interference pattern* between two known long-period cycles produces time-dependent residuals not fully captured by standard IAU precession corrections.

A further methodological caveat applies to modern measurements specifically: the reported  $575.31''/\text{cy}$  comes from fitting a GR-inclusive ephemeris to spacecraft ranging data

(Park et al. 2017 fit Mercury’s orbit jointly with all planets, 343 asteroids, and the PPN parameter  $\beta$ , finding  $\beta \approx 1$ ). This is conceptually equivalent to measuring the Newtonian baseline ( $\sim 532''/\text{cy}$ ) and adding the assumed GR contribution ( $\sim 43''/\text{cy}$ ). If BepiColombo applies the same GR-inclusive analysis, any change in the underlying perihelion advance from frame effects may be absorbed into a slightly different best-fit  $\beta$ , into residuals, or into the orbital baseline — rather than appearing as a clean drift in the reported total. A definitive test of the model’s prediction requires reporting the raw measured perihelion advance independent of an assumed GR baseline, or explicitly tracking the Newtonian and GR contributions separately between epochs.

### Part III: Predictions and Validation

## 12. Unified Predictive Formulas

A unified  $\sim 2,400$ -term formula system (planet-specific term counts 2,393–2,435) predicts the precession fluctuation of all seven planets (excluding Earth, the observer) using only time as input — no observation of each planet’s perihelion is required. The system uses Earth’s formulas (perihelion longitude, obliquity, eccentricity, Earth Rate Deviation) to predict how each planet’s *apparent* precession changes due to Earth’s reference frame motion.

**Table 25:** Unified predictive formula performance

Planet	$R^2$	RMSE ( $''/\text{cy}$ )	Base ( $''/\text{cy}$ )	Period (yr)
Mercury	0.999999	0.0974	531.4	243,867( $H \times 8/11$ )
Venus	0.999997	0.9160	-289.9	-447,089( $-8H/6$ )
Mars	0.999999	0.0980	1,690.9	76,644( $H \times 8/35$ )
Jupiter	0.999999	0.0975	1,932.5	67,063( $H/5$ )
Saturn	1.000000	0.0977	-3,092.0	$\sim 41,915(H/8, \text{retr.})$
Uranus	0.999998	0.1027	1,159.5	$\sim 111,772(H/3)$
Neptune	0.999985	0.0978	193.2	670,634( $H \times 2$ )

### 12.1 Eccentricity-Dependent Driver Mechanisms

The analysis reveals that different planets show fundamentally different fluctuation drivers:

- **Mercury** ( $e = 0.206$ ): Well-defined perihelion. Fluctuation range  $-180$  to  $+202''/\text{cy}$ , dominated by geometric modulation — angular interference of Earth’s and Mercury’s perihelion precessions.
- **Venus** ( $e = 0.007$ ): Poorly defined perihelion. Fluctuation range  $-1,353$  to  $+1,231''/\text{cy}$  —  $\sim 7\times$  larger than Mercury’s despite Venus being more circular — dominated by quadratic Earth Rate Deviation effects.
- **Mars through Neptune**: Smaller fluctuation ranges ( $-59$  to  $+60''/\text{cy}$  for Neptune up to  $-299$  to  $+288''/\text{cy}$  for Saturn), dominated by linear rate-cycle interactions.

This eccentricity dependence is a natural consequence of the reference frame interpretation: a planet whose perihelion is well-defined (eccentricity not too small) shows geometric modulation projecting onto a clear direction; a planet whose perihelion is essentially arbitrary ( $e \rightarrow 0$ ) primarily reflects Earth’s own rate variations, not its own geometry.

### 12.2 Saturn as the Obliquity Driver

Saturn is the only planet requiring time-varying obliquity and eccentricity parameters for accurate predictions. Its precession period ( $\sim 41,915$  years =  $H/8$ ) exactly equals Earth’s obliquity cycle — a resonance, not a coincidence. Without time-varying coupling terms, Saturn’s formula cannot achieve  $R^2 = 1.0$ , suggesting Saturn’s precession directly modulates Earth’s axial tilt oscillation.

## 13. Calibration, Validation, and Transparency

### 13.1 Free Parameters

The model has 6 adjustable parameters — 5 for the Earth simulation and 1 discrete configuration choice for the planetary Fibonacci structure:

**Table 26:** Free parameters

Parameter	Value	How determined
Earth Fundamental Cycle	335,317 yr	Fitted to 1246.03125 AD alignment + J2000 longitude
Fibonacci divisors	3, 8, 13	Structural assumption
Mean obliquity	23.41354°	Fitted to observed obliquity range
Amplitude	0.63603°	Fitted to observed obliquity range
Anchor year	-302, 635	Derived from Earth Fundamental Cycle and 1246.03125 AD
Planet configuration	Config #11	Exhaustive search; unique mirror-symmetric solution

The planet configuration assigns three quantities to each planet: an oscillation period (from Law 1’s Fibonacci hierarchy), a quantum number  $d$  (determining amplitude via Law 2), and a balance group (in-phase or anti-phase). The periods and balance groups are observationally constrained; only the  $d$ -assignment is a free choice, making this a single discrete parameter.

**Table 27:** Genuine predictions (not used in calibration)

Prediction	Model	Reference value	Agreement
Obliquity at 9,233 BC	24.5115°	24.1956° (La2004)	$\pm 0.32^\circ$
Obliquity at 11,725 AD	22.5435°	22.6117° (La2004)	$\pm 0.07^\circ$
Perihelion long. 1000 AD	85.764°	85.788° (Meeus)	$\pm 0.025^\circ$
Eccentricity (J2000)	0.01671	0.01671022 (NASA)	$\pm 0.00001$
Incl. to inv. plane	1.57869°	1.57869° (S&S 2012)	$\pm 0.0001^\circ$

### 13.2 Ascending Node Calibration

The inclination oscillation formula requires accurate ascending node positions on the invariable plane. Souami & Souchay (2012) published these for all planets, but a systematic issue arises: their values are calibrated to epoch-specific inclinations, while the model uses mean (time-averaged) inclinations. When Earth’s mean inclination ( $1.48113^\circ$ ) is used instead of the J2000 value ( $1.579^\circ$ ), the original S&S ascending nodes produce ecliptic inclinations that deviate from observed JPL values. Using spherical trigonometry:

$$\cos(i_{\text{ecl}}) = \cos(i_p) \cos(i_e) + \sin(i_p) \sin(i_e) \cos(\Delta\Omega) \quad (25)$$

where  $i_p$  and  $i_e$  are the planet’s and Earth’s inclinations to the invariable plane, and  $\Delta\Omega$  is the ascending node difference. Since  $i_{\text{ecl}}$  is known from JPL observations, the ascending node becomes the only unknown — geometrically determined, not a free parameter. Two independent methods — numerical optimization and analytical solution — produce identical results (Table 28).

**Table 28:** Ascending node calibration results

Planet	S&S (°)	Verified (°)	$\Delta$ (°)	JPL (°)	Error
Mercury	32.22	32.83	+0.61	7.005	< 0.0001°
Venus	52.31	54.70	+2.39	3.395	< 0.0001°
Mars	352.95	354.87	+1.92	1.850	< 0.0001°
Jupiter	306.92	312.89	+5.97	1.303	< 0.0001°
Saturn	122.27	118.81	-3.46	2.489	< 0.0001°
Uranus	308.44	307.80	-0.64	0.773	< 0.0001°
Neptune	189.28	192.04	+2.76	1.770	< 0.0001°

The calibration combines two independent datasets: JPL ecliptic inclinations from spacecraft tracking, and S&S invariable plane inclinations from angular momentum calculations. The ascending node is the geometric quantity that links them — uniquely determined by spherical trigonometry.

### 13.3 Historical Observation Validation

The 3D simulation has been validated against over 700 historical astronomical observations spanning ~2000 BC to ~4000 AD: Mercury and Venus transits (~190 events), Mars oppositions (~140), Jupiter–Saturn great conjunctions (~150), and mutual planetary occultations (~100). Accuracy: < 1' for the current epoch ( $\pm 100$  yr), < 5' for historical ( $\pm 1,000$  yr), < 15' for ancient ( $> 2,000$  yr). Against JPL Horizons and historical transit/opposition data (~1800–2200 AD), per-planet RMS accuracy is: Sun 0.003°, Moon 0.002°, Mercury 0.079°, Venus 0.041°, Mars 0.090°, Jupiter 0.052°, Saturn 0.072°, Uranus 0.016°, Neptune 0.004°.

### 13.4 Comparison with JPL DE440/441

The JPL Development Ephemeris (DE440/441; [Park et al. 2021](#)) is the gold standard for solar system dynamics, with independent confirmation from INPOP ([Fienga et al., 2011](#)) and EPM ([Pitjeva, 2010](#)) ephemerides.

**Table 29:** Obliquity predictions: model vs. La2004 ([Laskar et al., 2004](#))

Year	Model	La2004	Diff.
1000 BC	23.8253°	23.8144°	+0.011°
J2000	23.4393°	23.4393°	0 (calib.)
3000 AD	23.3103°	23.3099°	+0.0004°
5000 AD	23.0650°	23.0639°	+0.001°
7000 AD	22.8508°	22.8553°	-0.005°
10,000 AD	22.6182°	22.6534°	-0.04°
12,000 AD	22.5358°	22.6081°	-0.07°
20,000 AD	22.7692°	23.0630°	-0.29°

The model and La2004 agree within 0.001–0.01° from -1,000 BC through 5,000 AD — essentially exact over this 6 kyr window. Agreement remains within 0.1° from 7,000 AD through 12,000 AD. By 20,000 AD the two diverge by ~0.29°, with La2004 oscillating back upward while the model continues its bounded  $H/8$  cycle.

**Table 30:** Eccentricity predictions: model vs. [Laskar et al. 2004](#) — the primary differentiating prediction

Year	Model	<a href="#">Laskar et al. 2004</a>	Diff.
J2000	0.01671	0.01670	+0.00001
5,000 AD	0.01602	0.01534	+0.00068
11,725 AD	0.01403 (min)	0.01156	+0.00247
27,000 AD	0.01562	0.00263 (near min)	+0.01299

The model predicts eccentricity minimum of ~0.0140 at 11,725 AD versus Laskar’s continued decrease toward 0.00263 near 27,000 AD — a divergence larger than the current eccentricity itself. For timescales beyond ~2,000 years, neither the model nor DE440/441 can be directly verified — both are extrapolations.

### 13.5 Error Analysis

Uncertainties propagate from the 6 free parameters. The dominant source is the obliquity amplitude ( $\pm 0.01^\circ$ ), which grows linearly with time. [Table 31](#) shows propagated uncertainties at two future epochs.

**Table 31:** Propagated uncertainties at future epochs

Epoch	Obliquity	Eccentricity
Yr 3000 (J2000 + 1 ka)	23.3103° $\pm$ 0.02°	0.0166 $\pm$ 0.0001
Yr 12000 (J2000 + 10 ka)	22.5358° $\pm$ 0.2°	0.0140 $\pm$ 0.001

## 14. Testable Predictions

The model generates 19 specific predictions:

### 14.1 Near-Term (Decades)

- Mercury perihelion anomaly:** Geocentric precession will decrease from its J2000 value of ~5,598.26"/cy. BepiColombo (science operations from April 2027) provides the near-term test *provided the analysis pipeline reports the raw perihelion advance rather than a GR-inclusive ephemeris fit total* ([Section 11](#), [Table 24](#); caveat in [§11.5](#)).
- RA at maximum declination:** The Sun’s ICRF right ascension at summer solstice peaked at exactly 6h in 1246 AD and is now shifting.
- Jupiter and Saturn perihelion trends:** Current trends will continue without pattern change. Saturn’s perihelion precession rate will remain ecliptic-retrograde at ~-3,100 to -3,400"/cy indefinitely ([Section 6.1](#)). The Great Inequality theory predicts the rate should reverse within ~450 years.
- No major Planet Nine** (key differentiator): The 4-mirror-pair Fibonacci structure ([Laws 3 and 5](#), [§4 and 5](#)) forbids a long-term resident at hundreds of AU more massive than  $\sim 10^{-3} M_\oplus$  (Pluto-mass scale). A canonical 1.2-billion-evaluation balance search confirms that the best 9-planet min(Law 3, Law 5) balance achievable with a  $5 M_\oplus$  body at 450 AU is ~9%, vs. the 8-planet baseline of 99.9975% on Law 3 and 99.8632% on Law 5. The Vera Rubin Observatory (LSST, 2025–2035) discriminates against the conventional [Batygin & Brown hypothesis \(Batygin & Brown, 2016\)](#) of 4–10  $M_\oplus$  at 290–700 AU — itself contested by the OSSOS null result ([Lawler et al., 2017](#)) and over a decade of non-detection.

## 14.2 Medium-Term (Centuries)

5. **Axial precession period:** Currently below the mean ( $\sim 25,771$  vs  $\sim 25,794$  yr, i.e. precessing faster than average) and still decreasing. The model predicts a minimum of  $\sim 25,312$  yr around  $\sim 12,431$  AD ( $\sim 482$  yr below the  $H/13$  mean), followed by a maximum of  $\sim 26,051$  yr around  $\sim 32,340$  AD ( $\sim 257$  yr above the mean), continuing to oscillate on the perihelion precession cycle. The Capitaine formula is a polynomial extrapolation that does not model this oscillation.
6. **Obliquity divergence** after the next minimum ( $\sim 13,665$  AD at  $\sim 22.51^\circ$ ): model predicts a reversal back toward the mean on its  $H/8 = \sim 41,915$ -yr cycle, while standard polynomial extrapolations continue to diverge. Long-term envelope:  $22.21^\circ - 24.72^\circ$ .
7. **Longitude of perihelion divergence** after  $\sim 3,000$  AD.
8. **Gregorian calendar drift:** June solstice slips from June 21 (J2000) to June 17 by  $\sim 11,725$  AD — a  $\sim 4$ -day shift driven by the Gregorian year (365.2425 d) running slightly long against the model's solar year ( $\sim 365.2422$  d) plus secular changes in obliquity, eccentricity, and the equation of centre.
9. **Analemma shape changes:** the figure-8 shifts forward with the perihelion precession cycle, its *width* oscillates with eccentricity ( $H/16 = \sim 20,957$  yr cycle) and its *length* oscillates with obliquity ( $H/8 = \sim 41,915$  yr cycle).

## 14.3 Long-Term (Millennia)

10. **Eccentricity minimum at  $\sim 11,725$  AD:**  $\sim 0.0140$ , then increasing. Key differentiator from Milankovitch theory.
11. **Inclination minimum at  $\sim 32,682$  AD:**  $\sim 0.845^\circ$  to the invariable plane (the next balanced year, one full Earth Fundamental Cycle after the previous one). Earth's inclination then rises again on its  $H$ -year cycle. Standard polynomial extrapolations predict continued decrease without a defined minimum.
12. **Length of Day variation:** LOD will slightly increase until  $\sim 6,000$  AD, then decrease until  $\sim 23,000$  AD.
13. **Solar year in days:** Will decrease until  $\sim 12,300$  AD.
14. **Sidereal year in seconds:** Fixed at 31,558,149.76 s.
15. **Precession periods locked to  $8H$ :** All planetary perihelion, axial, and obliquity periods will remain expressible as integer divisors of  $8H = 2,682,536$  yr (the Solar System Resonance Cycle).
16. **Invariable plane tilt:** Mean =  $1.48113^\circ$  with  $\pm 0.63603^\circ$  amplitude.
17. **Orbital cooling onset and next glaciation peak:** The  $8H$  Orbital Forcing Formula (§10.4) predicts a peak orbital interglacial warmth at  $\sim 5,700$  yr from now ( $\sim 7,700$  AD) at  $C(t) \approx -0.56$ , followed by sustained orbital cooling. The signal crosses zero (transitioning from interglacial-favoring to glacial-favoring) at  $\sim 32,300$  yr from now ( $\sim 34,300$  AD), and the first glacial maximum follows at  $\sim 38,000$  yr from now ( $\sim 40,000$  AD); the strongest glaciation in the next quarter-million years sits at  $\sim 194,500$  yr from now. Intervals between predicted glacial peaks cluster at  $\sim 40$  kyr (obliquity band) rather than the  $\sim 100$  kyr pacing of the past  $\sim 700$  kyr: the next 250 kyr orbital signal resembles a pre-MPT

“41-kyr world” more than the late-Pleistocene 100-kyr regime, consistent with Berger & Loutre (2002)'s “exceptionally long interglacial ahead” prediction. These describe orbital-clock phase transitions, not direct surface-temperature predictions — the surface response can lag the orbital signal by several kyr (compare the formula's  $-9$  kyr LGM-timing offset, §10.4) and depends on whether post-MPT ice-sheet hysteresis tracks the new orbital pacing. Anthropogenic  $\text{CO}_2$  may delay the next natural glaciation by 50+ kyr in moderate-emission scenarios (Ganopolski et al., 2016); this anthropogenic effect is not included in the formula.

18. **Long-term temperature decline:** As inclination tilt decreases, longer glacial periods.
19. **Planet obliquity cycles:** Every planet follows the same two-component formula as Earth (Eq. 16), with amplitude from Law 2. Three cycles are confirmed (Mercury 0.2%, Earth 2%, Mars 2.4%); three remain testable (Jupiter, Saturn, Uranus); Venus and Neptune have obliquity cycle = ICRF period, so the two components cancel exactly  $\rightarrow$  constant obliquity. See Table 11 for all values.

## 14.4 Falsification Criteria

Each major claim of the model maps to a specific falsifier and observational test. The model would be falsified if any of the following outcomes is observed:

**Table 32:** Falsification criteria: each major claim mapped to its specific falsifier and observational test.

Claim	Falsifier	Test
Bounded eccentricity oscillation (Earth-Saturn coupling, §5)	Eccentricity continues monotonic decline toward $\sim 0$ as Milankovitch theory predicts, rather than reaching a bounded minimum near $\sim 0.0140$ at $\sim 11,725$ AD	Millennia of continued tracking
100,000-yr climate cycle belongs to the inclination-side family (§10); empirical centroid is the Mercury-Mars $s_1 - s_4$ nodal beat at 107.3 kyr	Direct eccentricity forcing confirmed: bispectral 95k+125k coupling detected and 405-kyr term at predicted dominant amplitude in post-MPT LR04	Continued LR04 / longer non-tuned record analysis
Mercury reference-frame effect (§11)	Geocentric precession remains constant at $\sim 5,604''/\text{cy}$ over decades	BepiColombo science operations, April 2027
No major Planet Nine (Laws 3 + 5 balance closure)	Body more massive than $\sim 0.1 M_\oplus$ found at hundreds of AU in long-term resident orbit	Vera Rubin / LSST 2025–2035

**Structural assumption.** Several of these falsifiers — the Saturn ecliptic-retrograde permanence (§6.1), the Mercury reference-frame effect (§11), and the no-major-Planet-Nine

claim — depend on treating the Fibonacci balance as *predictive*: the closure of the 8-planet structure is a real physical constraint that forbids deviations. If the structure were merely *descriptive* (a coincidence fit to the 8 planets we happen to observe), then a future detection inconsistent with these claims could be accommodated by re-fitting the Fibonacci  $d$ -values rather than falsifying the framework. The model’s broader claim — formation-epoch freezing of KAM-stable Fibonacci configurations (§7) — treats the balance as predictive; the BepiColombo and LSST results will discriminate which interpretation is correct.

## 15. Discussion

### 15.1 What the Model Explains

The Holistic Universe Model unifies six phenomena — axial precession, inclination precession, perihelion precession, obliquity variation, eccentricity variation, and day/year length changes — within a single geometric framework. Beyond Earth, six Fibonacci Laws connect the orbital properties of all eight planets through a single timescale. The framework produces closed-form formulas for any epoch, eliminating the need for numerical integration within its domain of applicability.

### 15.2 Relationship to Existing Theory

The model does not contradict Newtonian gravity. It proposes that the long-term behavior of planetary parameters may be captured by a geometric description that reveals Fibonacci structure — consistent with KAM theory’s prediction that maximally stable orbits have frequency ratios converging to the golden ratio. The formation-epoch mechanism (Section 7) provides a physical explanation: KAM-selected Fibonacci configurations were frozen during protoplanetary disk dissipation and preserved by conservative dynamics for 4.5 billion years.

### 15.3 Limitations

The model does not explain:

- **Why  $H = 335,317$**  specifically (the Fibonacci ratio 13:3 is understood via KAM theory, but the absolute timescale is empirical)
- Short-term perturbations or chaotic orbital evolution

The model describes secular (long-term) trends only. It does not include short-period perturbations that average to zero over millennial timescales:

**Table 33:** Physical effects not included in the model

Perturbation	Period	Effect	Treatment
Lunar nodal cycle	18.6 yr	$\pm 9''$ nutation	Averaged out
Chandler wobble	$\sim 433$ d	Axis wobble ( $0.7''$ )	Not modeled
Annual wobble	1 yr	Seasonal mass redistrib.	Not modeled
Jupiter perturbations	$\sim 11.86$ yr	Orbital variations	Averaged out
Saturn perturbations	$\sim 29.5$ yr	Orbital variations	Averaged out
Solar activity cycle	$\sim 11$ yr	Minor thermal effects	Not modeled

For the model’s primary predictions (obliquity, eccentricity, longitude of perihelion over millennia), these perturbations contribute  $< 0.01^\circ$  to obliquity,  $< 0.0001$  to eccentricity, and  $< 0.1^\circ$  to longitude — within the model’s stated uncertainties. For precise positions on any given day, standard ephemerides (JPL DE440/441) should be used. The

model’s configuration applies from  $\sim 1$  million years ago (Mid-Pleistocene Transition) to the present epoch.

### 15.4 The Overfitting Concern

With 6 free parameters (5 continuous, 1 discrete configuration), overfitting is addressed by:

1. Explicitly separating calibration from predictions (Section 13)
2. Agreement with values not used in construction (eccentricity, invariable plane inclination, ascending nodes to  $< 0.0001^\circ$ )
3. 19 testable predictions, several falsifiable within decades
4.  $R^2 > 0.9996$  for all 7 planets using a single formula structure
5. Six Fibonacci Laws predicting orbital properties with zero free parameters, with suggestive exoplanet parallels

## 16. Conclusions

We have presented six Fibonacci Laws of planetary motion derived from a unified geometric model. The laws connect a single timescale — the 335,317-year Earth Fundamental Cycle, produced by two counter-rotating reference points in a 13:3 ratio — to the orbital properties of all eight planets:

1. **Law 1:** The Earth Fundamental Cycle divided by Fibonacci numbers generates Earth’s major precession periods (a hierarchy unique to Earth)
2. **Law 2:** A single constant  $\psi$  (derived from Earth) predicts all eight inclination amplitudes from Fibonacci divisors and mass alone ( $d \times \text{amp} \times \sqrt{m} = \psi$ )
3. **Law 3:** Angular-momentum-weighted inclination oscillations balance to 99.9975% (with phase-derived base eccentricities)
4. **Law 4:** A single constant  $K$  (derived from Earth) predicts all eight eccentricity amplitudes from Fibonacci divisors, mass, distance, and mean obliquity:  $e_{\text{amp}} = K \times \sin(\text{mean obliquity}) \times \sqrt{d}/(\sqrt{m} \times a^{3/2})$  (Section 5.1)
5. **Law 5:** An independent eccentricity balance reaches 99.8632% from the same Fibonacci divisors, with base eccentricities derived from the System Reset phase ( $90^\circ$  in-phase,  $270^\circ$  Saturn); predicts Saturn’s eccentricity from the other seven planets to  $\sim 0.27\%$
6. **Law 6:** Earth’s  $H/8$  obliquity cycle equals both Jupiter’s ICRF perihelion and Saturn’s ecliptic perihelion — a triple identity at  $H/8$  closing through the Fibonacci identity  $3 + 5 = 8$

A significance analysis using a direct joint permutation test over the 4 empirical tests (model-independent; joint null captures inter-test correlation by construction) yields a combined  $p$ -value spanning  $1.5 \times 10^{-4}$  (permutation null) to  $1.0 \times 10^{-6}$  (MC nulls over 9 tests), equivalently 3.62–4.75  $\sigma$ . A leave-one-out jackknife confirms that all eight planets are required to reach the full significance: dropping any single planet reduces the combined signal, with Jupiter and Uranus being the most load-bearing. A physical origin mechanism explains the structure’s precision: KAM-selected Fibonacci configurations were frozen during protoplanetary disk dissipation and preserved by conservative dynamics for 4.5 billion years.

These laws produce specific consequences for Earth: a unified obliquity formula tracking standard theory to within

$\sim 0.5^\circ$  over  $\pm 20,000$  years (and predicting bounded oscillation in the  $22.21^\circ$ – $24.72^\circ$  envelope where polynomial extrapolations diverge), a  $\sim 20,957$ -year eccentricity cycle reaching its next minimum at  $\sim 11,725$  AD, a reinterpretation of the 100,000-year glacial cycle as belonging to the inclination-side family of eigenmode beats with empirical centroid at the Mercury–Mars  $s_1 - s_4$  nodal beat at 107 kyr (and the model’s  $H/3$  inclination precession as one theoretical pathway within that family) supported by the 8H Orbital Forcing Formula ( $R^2 = 0.238$  on LR04, with forward projection placing the next natural glaciation peak at  $\sim 38,000$  yr from now), a decreasing Mercury perihelion anomaly testable by Bepi-Colombo ( $\sim 574.61''/\text{cy}$  versus MESSENGER’s  $575.31''/\text{cy}$ , science operations from April 2027), and a new explanation for Saturn’s ecliptic-retrograde perihelion precession ( $\sim -3,372''/\text{cy}$  geocentric predicted versus  $\sim -3,400''/\text{cy}$  observed). The Milankovitch beat frequency structure reveals that all five standard precession cycles emerge as  $H/n$  with Fibonacci-related indices, with the Fibonacci subtraction property guaranteeing physical closure of the beat equations.

A unified  $\sim 2,400$ -term formula system (planet-specific term counts 2,393–2,435) predicts planetary precession with  $R^2 > 0.99998$  for all 7 planets (Table 25). The model uses 6 free parameters and is fully transparent about calibration versus prediction.

## Acknowledgments

The author thanks the developers of JPL Horizons, WebGeocalc, and the IAU standards for providing the observational data upon which this model is built. The interactive 3D simulation was built using Three.js.

## Data Availability

All data, formulas, and calculation scripts underlying this work are publicly available:

- Model documentation: <https://holisticuniverse.com>
- Interactive 3D simulation: <https://3d.holisticuniverse.com>
- Data visualization: <https://data.holisticuniverse.com>
- Source code, predictive formula scripts, significance tests, and technical docs: <https://github.com/dvansonsbeek/3d>

## Conflict of Interest

The author declares no conflicts of interest. This research received no external funding.

## References

- Aschwanden, M. J. (2018). Self-organizing systems in planetary physics: Harmonic resonances of planet and moon orbits. *New Astronomy*, 58, 107–123.
- Backus, G. (1969). Critique of “The Resonant Structure of the Solar System” by A. M. Molchanov. *Icarus*, 11, 88–92.
- Barker, S., Lisiecki, L. E., Knorr, G., Nuber, S., & Tzedakis, P. C. (2025). Distinct roles for precession, obliquity, and

eccentricity in Pleistocene 100-kyr glacial cycles. *Science*, 387(6737), eadp3491.

- Batygin, K., & Brown, M. E. (2016). Evidence for a Distant Giant Planet in the Solar System. *Astronomical Journal*, 151, 22.
- Berche, B., & Medina, E. (2024). The advance of Mercury’s perihelion: a historical review. *arXiv:2402.04643*.
- Berger, A. (1978). Long-term variations of daily insolation and Quaternary climatic changes. *Journal of the Atmospheric Sciences*, 35, 2362–2367.
- Berger, A. (1988). Milankovitch theory and climate. *Reviews of Geophysics*, 26(4), 624–657.
- Berger, A. & Loutre, M. F. (2002). An exceptionally long interglacial ahead? *Science*, 297(5585), 1287–1288.
- Bills, B. G. (2005). Forced obliquity variations of Mercury. *Journal of Geophysical Research*, 110, E04006.
- Boulila, S., Vahlenkamp, M., De Vleeschouwer, D., et al. (2020). Toward a robust and consistent middle Eocene astronomical timescale. *Palaeogeography, Palaeoclimatology, Palaeoecology*, 549, 109702.
- Capitaine, N., Wallace, P. T., & Chapront, J. (2003). Expressions for IAU 2000 precession quantities. *Astronomy & Astrophysics*, 412, 567–586.
- Chapront, J., Chapront-Touzé, M., & Francou, G. (2002). Expressions for the Celestial Intermediate Pole and Celestial Ephemeris Origin consistent with the IAU 2000A precession-nutation model. *Astronomy & Astrophysics*, 387, 700–709.
- Cheng, H., Edwards, R. L., Sinha, A., et al. (2016). The Asian monsoon over the past 640,000 years and ice age terminations. *Science*, 352, 343–347.
- Clemence, G. M. (1947). The relativity effect in planetary motions. *Reviews of Modern Physics*, 19(4), 361–364.
- Cottureau, L., & Souchay, J. (2009). Rotation of rigid Venus: a complete precession-nutation model. *Astronomy & Astrophysics*, 507, 1635–1648.
- Farley, K. A. (1995). Cenozoic variations in the flux of interplanetary dust recorded by  $^3\text{He}$  in a deep-sea sediment. *Nature*, 376, 153–156.
- Fienga, A., Laskar, J., Kuchynka, P., et al. (2011). The INPOP10a planetary ephemeris and its applications in fundamental physics. *Celestial Mechanics and Dynamical Astronomy*, 111, 363–385.
- Ganopolski, A., Winkelmann, R. & Schellnhuber, H. J. (2016). Critical insolation–CO<sub>2</sub> relation for diagnosing past and future glacial inception. *Nature*, 529, 200–203.
- Greene, J. M. (1979). A method for determining a stochastic transition. *Journal of Mathematical Physics*, 20(6), 1183–1201.

- Grimm, S. L., Demory, B.-O., Gillon, M., et al. (2018). The nature of the TRAPPIST-1 exoplanets. *Astronomy & Astrophysics*, 613, A68.
- Harkness, W. (1891). *The Solar Parallax and Its Related Constants* (Washington: Government Printing Office).
- Hays, J. D., Imbrie, J., & Shackleton, N. J. (1976). Variations in the Earth's orbit: Pacemaker of the ice ages. *Science*, 194(4270), 1121–1132.
- Iorio, L. (2009). The recently determined anomalous perihelion precession of Saturn. *The Astronomical Journal*, 137, 3615–3618.
- Kawamura, K., Parrenin, F., Lisiecki, L., et al. (2007). Northern Hemisphere forcing of climatic cycles in Antarctica over the past 360,000 years. *Nature*, 448, 912–916.
- Konopliv, A. S., Park, R. S., Rivoldini, A., et al. (2021). Mars precession rate determined from radiometric tracking of the InSight Lander. *Planetary and Space Science*, 199, 105208.
- Laskar, J. (1989). A numerical experiment on the chaotic behaviour of the Solar System. *Nature*, 338, 237–238.
- Laskar, J. (1993). Orbital, precessional and insolation quantities for the Earth from  $-20$  Myr to  $+10$  Myr. *Astronomy & Astrophysics*, 270, 522–533.
- Laskar, J. (1997). Large scale chaos and the spacing of the inner planets. *Astronomy & Astrophysics*, 317, L75–L78.
- Laskar, J., Robutel, P., Joutel, F., et al. (2004). A long-term numerical solution for the insolation quantities of the Earth. *Astronomy & Astrophysics*, 428, 261–285.
- Laskar, J., Fienga, A., Gastineau, M., & Manche, H. (2011). La2010: A new orbital solution for the long-term motion of the Earth. *Astronomy & Astrophysics*, 532, A89.
- Lawler, S. M., Shankman, C., Kavelaars, J. J., et al. (2017). OSSOS VIII: The transition between the two extreme outer solar system populations. *Astronomical Journal*, 153, 33.
- Li, G., Xia, Y., & Zhou, J.-L. (2019). The inclination of the invariable plane of the solar system: the contribution of trans-Neptunian objects. *arXiv:1909.11293*.
- Lisiecki, L. E., & Raymo, M. E. (2005). A Pliocene–Pleistocene stack of 57 globally distributed benthic  $\delta^{18}\text{O}$  records. *Paleoceanography*, 20, PA1003.
- Mecheri, R., & Abdelatif, T. (2022). Secular Variations of the Sun's Gravitational Quadrupole Moment and Their Impact on GR Tests. *Remote Sensing*, 14(19), 4798.
- Meeus, J. (1998). *Astronomical Algorithms*, 2nd edn. (Richmond: Willmann-Bell).
- Mitchell, R. N., & Kirscher, U. (2023). Mid-Proterozoic day length stalled by tidal resonance. *Nature Geoscience*, 16, 567–569.
- Morbidelli, A., & Giorgilli, A. (1995). Superexponential stability of KAM tori. *Journal of Statistical Physics*, 78, 1607–1617.
- Muller, R. A., & MacDonald, G. J. (1997a). Glacial cycles and astronomical forcing. *Science*, 277, 215–218.
- Muller, R. A., & MacDonald, G. J. (1997b). Spectrum of 100-kyr glacial cycle: Orbital inclination, not eccentricity. *Proceedings of the National Academy of Sciences*, 94, 8329–8334.
- Newcomb, S. (1898). *Tables of the Motion of the Earth on its Axis and Around the Sun*, Astronomical Papers, Vol. VI (Washington: US Naval Observatory).
- Park, R. S., Folkner, W. M., Konopliv, A. S., et al. (2017). Precession of Mercury's perihelion from ranging to the MESSENGER spacecraft. *The Astronomical Journal*, 153(3), 121.
- Park, R. S., et al. (2021). The JPL planetary and lunar ephemerides DE440 and DE441. *The Astronomical Journal*, 161(3), 105.
- Peale, S. J. (2006). The free precession and libration of Mercury. *Icarus*, 178, 4–18.
- Petit, J. R., Jouzel, J., Raynaud, D., et al. (1999). Climate and atmospheric history of the past 420,000 years from the Vostok ice core, Antarctica. *Nature*, 399, 429–436.
- Pitjeva, E. V. (2010). EPM ephemerides and relativity. *Proceedings of the IAU Symposium*, 261, 170–178.
- Pitjeva, E. V., & Pitjev, N. P. (2013). Relativistic effects and dark matter in the Solar system from observations of planets and spacecraft. *Monthly Notices of the Royal Astronomical Society*, 432, 3431–3437.
- Pletser, V. (2019). Fibonacci numbers and the golden ratio in biology, physics, astrophysics, chemistry and technology: a non-exhaustive review. *Astrophysics and Space Science*, 364, 158.
- Ridgwell, A. J., Watson, A. J., & Raymo, M. E. (1999). Is the spectral signature of the 100 kyr glacial cycle consistent with a Milankovitch origin? *Paleoceanography*, 14(4), 437–440.
- Rogoszinski, Z., & Hamilton, D. P. (2020). Tilting Ice Giants with a Spin–Orbit Resonance. *The Astrophysical Journal*, 888, 60.
- Saillenfest, M., Lari, G., & Courtot, A. (2020). The future large obliquity of Jupiter. *Astronomy & Astrophysics*, 640, A11.
- Saillenfest, M., Lari, G., Boué, G., & Courtot, A. (2021). The large obliquity of Saturn explained by the fast migration of Titan. *Nature Astronomy*, 5, 345–349.
- Saillenfest, M., Rogoszinski, Z., Lari, G., et al. (2022). Tilting Uranus via the migration of an ancient satellite. *Astronomy & Astrophysics*, 668, A108.

- Smulsky, J. J. (2011). New components of the Mercury's perihelion precession. *Natural Science*, 3(4), 268–274.
- Souami, D., & Souchay, J. (2012). The solar system's invariable plane. *Astronomy & Astrophysics*, 543, A133.
- Standish, E. M., & Williams, J. G. (1992). Keplerian Elements for Approximate Positions of the Major Planets. JPL Solar System Dynamics, [https://ssd.jpl.nasa.gov/planets/approx\\_pos.html](https://ssd.jpl.nasa.gov/planets/approx_pos.html).
- Veres, D., et al. (2013). The Antarctic ice core chronology (AICC2012). *Climate of the Past*, 9, 1733–1748.
- Vervoort, P., Nair, S., Luger, R., Agol, E., & Barnes, R. (2022). System Architecture and Planetary Obliquity: Implications for Long-term Habitability. *The Astronomical Journal*, 164, 130.
- Vondrák, J., Capitaine, N., & Wallace, P. (2011). New precession expressions, valid for long time intervals. *Astronomy & Astrophysics*, 534, A22.
- Willeit, M., Ganopolski, A., Calov, R., & Brovkin, V. (2019). Mid-Pleistocene transition in glacial cycles explained by declining CO<sub>2</sub> and regolith removal. *Science Advances*, 5(4), eaav7337.
- Wilson, C. (1985). The great inequality of Jupiter and Saturn: from Kepler to Laplace. *Archive for History of Exact Sciences*, 33, 15–290.